TECHNICAL REVIEW

No. 1 – 2012

High-resolution Fly-over Beamforming
Clustering Approaches to Automatic Modal Parameter Estimation

www.bksv.com

Brüel & Kjær

Previously issued numbers of Brüel & Kjær Technical Review

1 – 2011 Performance Investigation of the Dual-Layer Array (DLA) at Low Frequencies
Calculating the Sound Field in an Acoustic Intensity Probe Calibrator – A Practical Utilisation of Boundary Element Modelling
Multi-field Microphone – When the Sound Field is Unknown

1 – 2010 Time Selective Response Measurements – Good Practices and Uncertainty
Measurement of Absorption Coefficient, Radiated and Absorbed Intensity on the Panels of a Vehicle Cabin using a Dual Layer Array with Integrated Position Measurement
ISO 16063 – 11: Uncertainties in Primary Vibration Calibration by Laser Interferometry – Reference Planes and Transverse Motion

1 – 2009 Use of Volume Velocity Sound Sources in the Measurement of Acoustic Frequency Response Functions
Turnkey Free-field Reciprocity System for Primary Microphone Calibration

1 – 2008 ISO 16063–11: Primary Vibration Calibration by Laser Interferometry: Evaluation of Sine Approximation Realised by FFT
Infrasound Calibration of Measurement Microphones
Improved Temperature Specifications for Transducers with Built-in Electronics

1 – 2007 Measurement of Normal Incidence Transmission Loss and Other Acoustical Properties of Materials Placed in a Standing Wave Tube

1 – 2006 Dyn-X Technology: 160 dB in One Input Range
Order Tracking in Vibro-acoustic Measurements: A Novel Approach Eliminating the Tacho Probe
Comparison of Acoustic Holography Methods for Surface Velocity Determination on a Vibrating Panel

1 – 2005 Acoustical Solutions in the Design of a Measurement Microphone for Surface Mounting
Combined NAH and Beamforming Using the Same Array
Patch Near-field Acoustical Holography Using a New Statistically Optimal Method

1 – 2004 Beamforming

1 – 2002 A New Design Principle for Triaxial Piezoelectric Accelerometers
Use of FE Models in the Optimisation of Accelerometer Designs
System for Measurement of Microphone Distortion and Linearity from Medium to Very High Levels

(Continued on cover page 3)

Technical Review

No. 1 – 2012

Contents

Editor: Harry K. Zaveri

High-resolution Fly-over Beamforming Using a Small Practical Array*

*Jorgen Hald†, Yutaka Ishii‡, Tatsuya Ishii**, Hideshi Oinuma**, Kenichiro Nagai**, Yuzuru Yokokawa** and Kazuomi Yamamoto***

Abstract

This paper describes a commercially available fly-over beamforming system based on methodologies already published, but using an array that was designed for quick and precise deployment on a concrete runway rather than for minimum sidelobe level. Time domain tracking Delay And Sum (DAS) beamforming is the first processing step, followed by Deconvolution in the frequency domain to reduce sidelobes, enhance resolution, and get absolute scaling of the source maps. The system has been used for a series of fly-over measurements on a Business Jet type MU300 from Mitsubishi Heavy Industries. Results from a couple of these measurements are presented: contribution spectra from selected areas on the aircraft to the sound pressure level at the array are compared against the total sound pressure spectrum measured by the array. One major aim of the paper is to verify that the system performs well although the array was designed with quick deployment as a main criterion. The results are very encouraging. A second aim is to elaborate on the handling of the array-shading function in connection with the calculation of the Point Spread Function (PSF) used in deconvolution. Recent publications have used a simple formula to compensate for Doppler effects for the case of flat broadband spectra. A more correct formula is derived in this paper, also covering a Doppler correction to be made in the shading function, when that function is used in the PSF calculation.

---

* First published in Proc. 33rd AIAA Aeroacoustics Conference, 2012

† Brüel & Kjær, Denmark.

‡ Brüel & Kjær Japan.

** JAXA (Japan Aerospace Exploration Agency), Japan.

Résumé

Cet article concerne un système à formation de faisceau pour mesures acoustiques de survols d'aéronefs, disponible dans le commerce et qui, intégrant des méthodologies ayant déjà fait l'objet de publications, est doté d'une antenne acoustique plus conçue au départ pour être déployée rapidement et avec précision sur une piste en béton que pour minimiser les niveaux de lobe secondaire. La technique de formation de faisceau, avec suivi des délais temporels et somme, constitue le premier volet de traitement du signal, précédant une déconvolution dans le domaine fréquentiel pour réduire les lobes latéraux, améliorer la résolution et obtenir une imagerie des sources en échelle absolue. Ce système a été utilisé pour les mesures de survol d'un avion à réaction MU300 du constructeur Mitsubishi Heavy Industries. Les résultats de quelques-unes de ces mesures sont présentés ici : les spectres associés à des zones spécifiques de l'aéronef et contribuant au niveau de pression acoustique sont comparés au spectre de pression acoustique total mesuré par l'antenne. Cet article vise avant tout à vérifier le fonctionnement correct de l'antenne au vu et en dépit du principal critère ayant présidé à sa conception, à savoir sa capacité à être déployée rapidement. Dans un deuxième temps, il étudie la manière dont est gérée la fonction d'ombre acoustique dans le calcul de la fonction PSF (dispersion de points) utilisée pour la déconvolution. Des publications récentes avaient utilisé une formule simple pour compenser les effets Doppler en cas de spectres bande large plats. Une formule plus exacte est ici présentée, qui couvre également la correction Doppler à appliquer à la fonction d'ombre acoustique lorsque cette fonction est utilisée pour le calcul de la PSF.

Zusammenfassung

Dieser Artikel beschreibt ein kommerziell erhältliches Beamforming-System für Überflugmessungen, das auf bereits veröffentlichter Methodik beruht, jedoch ein Array verwendet, das in erster Linie für den schnellen und präzisen Einsatz auf einer Landebahn aus Beton und weniger im Hinblick auf minimierte Nebenmaxima entwickelt wurde. Der erste Verarbeitungsschritt ist Delay-And-Sum-Beamforming im Zeitbereich, gefolgt von Dekonvolution (Entfaltung) im Frequenzbereich, um Nebenmaxima zu reduzieren, die Auflösung zu verbessern und eine absolute Skalierung der Quellenkarten zu erhalten. Das System wurde für eine Reihe von Überflugmessungen mit einem Business-Jet vom Typ MU300 von Mitsubishi Heavy Industries verwendet. Es werden Ergebnisse von einigen dieser Messungen präsentiert: Teilspektren von ausgewählten Bereichen am Flugzeug,

die zum Schalldruckpegel am Array beitragen, werden mit dem vom Array gemessenen Gesamtschalldruckspektrum verglichen. Ein wichtiges Anliegen des Artikels ist die Verifizierung, dass das System einwandfrei arbeitet, obwohl das Hauptkriterium bei der Konstruktion des Arrays seine schnelle Einsatzfähigkeit war. Die Ergebnisse sind sehr ermutigend. Ein weiteres Anliegen ist die detaillierte Behandlung der Array-Abschattungsfunktion in Verbindung mit der Berechnung der zur Entfaltung verwendeten Point Spread-Funktion (PSF). In neueren Veröffentlichungen wurde eine einfache Formel zur Kompensation der Doppler-Effekte für flache Breitbandspektren verwendet. Im vorliegenden Artikel wird eine korrektere Formel abgeleitet, die ebenfalls eine in der Abschattungsfunktion erforderliche Doppler-Korrektur umfasst, wenn diese Funktion bei der PSF-Berechnung verwendet wird.

Nomenclature

$b(t)$	= DAS beamformed time signal
$B(\omega)$	= DAS beamformed frequency spectrum
$B_{ij}(\omega)$	= DAS beamformed spectrum at focus point j due to model source i
c	= Propagation speed of sound
DAS	= Delay And Sum
Df_{mi}, Df_{mj}	= Doppler frequency shift factor at microphone m for signal from point i and j, respectively
f	= Frequency
$H_{ij}(\omega)$	= Element of Point Spread Function: From model source i to focus point j
i	= Index of monopole point source in Deconvolution source model, $i = 1, 2, \ldots, I$
I	= Number of focus/source points in calculation mesh
j	= Index of focus position, $j = 1, 2, \ldots, I$, *or* imaginary unit $\sqrt{-1}$
k	= Wavenumber ($k = \omega/c$)
κ	= Parameter defining steepness in radial cut-off of array shading filters
m	= Microphone index, $m = 1, 2, \ldots, M$
M	= Number of microphones
M_0	= Mach number
$p_m(t)$	= Sound pressure time signal from microphone m
$\hat{p}_m(t)$	= Shaded time signal for microphone m

$P_m(\omega)$ = Frequency spectrum from microphone m
$P_{mi}(\omega)$ = Frequency spectrum from microphone m due to model source i
PSF = Point Spread Function (2D spatial power response to a monopole point source)
Π_{model} = DAS beamformed pressure power (pressure squared) from the point source model in deconvolution
Π_{measured} = DAS beamformed pressure power from an actual measurement
$Q_i(\omega)$ = Amplitude spectrum of model point source i
$r_{mj}(t)$ = Distance from microphone m to moving focus point j
r_{mj} = Distance from microphone m to focus point j at the centre of an averaging interval
R_m = Distance of microphone m from array centre
$R_{\text{coh}}(\omega)$ = Frequency dependent radius of active sub-array
$s_{mi}(t)$ = Distance from microphone m to moving source point i
s_{mi} = Distance from microphone m to source point i at the centre of an averaging interval
s_{0i} = Distance from array centre to source point i at the centre of an averaging interval
$S_i(\omega)$ = Power spectrum of model point source i
t = Time
$\mathbf{U}$ = Aircraft velocity vector
U = Aircraft velocity, $U \equiv |\mathbf{U}|$
$w_m(\tau)$ = Delay domain shading function applied to microphone m
$W_m(\omega)$ = Shading function in frequency domain
ω = Angular frequency ($\omega = 2\pi f$)

Introduction

Beamforming has been widely used for noise source localization and quantification on aircraft during fly-over for more than a decade [1 – 6]. The standard Delay And Sum (DAS) beamforming algorithm, however, suffers from poor low-frequency resolution, sidelobes producing ghost sources, and lack of absolute scaling. A special scaling method was introduced in [2] to get absolute contributions. During recent years, deconvolution has been introduced as a post-processing step to scale the output contribution maps, but also improving both the low-frequency resolution and the sidelobe suppression [3 – 8]. For a planar distribution of incoherent monopole sources, which is a fairly good model for the

aerodynamic noise sources of an aircraft, the output of a DAS beamforming at a given frequency will be approximately equal to the true source power distribution convolved in 2D with a frequency-dependent spatial impulse response, which is called the Point Spread Function (PSF). The PSF is defined entirely by the array geometry and the relative positioning of the array and the source plane, so for stationary sources it can be easily calculated and used in a deconvolution algorithm to estimate the underlying real source distribution. A difficulty with the use of deconvolution in connection with fly-over measurements is the fact that the DAS beamforming algorithm must be implemented in the time domain in order to track the aircraft, while deconvolution algorithms work only in the frequency domain with the source at a fixed position relative to the array. Deconvolution in its basic form therefore cannot take Doppler shifts into account. A method to do that in an approximate and computationally efficient way was introduced in [3], further developed in [4] and applied with actual fly-over measurements in [5]. The method adapts the PSF to the output from a DAS measurement on a moving point source, assuming flat broadband source spectra. Under that assumption, the spectral shape will remain almost unchanged from the Doppler shifts. The method is able to compensate for the change in lobe pattern caused by Doppler shifts.

Most of the published applications of microphone arrays for fly-over measurement have been using rather large and complicated array geometries requiring considerable time to deploy and to measure the exact microphone positions. This paper describes an investigation of the possibility of building an array system that can be quickly deployed on a runway and quickly taken down again. The entire system including the array and the implemented processing methodology is described in “Method and System Overview” on page 6, and its performance is illustrated in “Application to MU300 Business-jet Fly-over” on page 16 by results from a series of fly-over measurements on a business jet. The calculation of the PSF is covered in some detail. A derivation of the Doppler corrected PSF is given in the Appendix, and it turns out to have a slightly different form than assumed in [3], [4] and [5], although it produces almost identical results when a frequency-independent array-shading function is used. “Accuracy of the Point Spread Function” on page 14 presents an investigation of the match between the analytical frequency domain PSF and the DAS response to a moving point source.

Method and System Overview

The applied method follows the same overall measurement and processing scheme as the hybrid time-frequency approach described in [5]. Aircraft position during a fly-over is measured with an onboard GPS system together with speed, roll, yaw and pitch. Synchronization with array data is achieved by recording an IRIG-B time-stamp signal together with the array data and also with the GPS data on the aircraft. The beamforming calculation is performed with a standard tracking time-domain DAS algorithm [2]. For each focus point in the moving system, FFT and averaging in short time intervals are then performed to obtain spectral noise source maps representing the aircraft positions at the middle of the averaging intervals. Diagonal Removal is implemented as described in [2], providing the capability of suppressing the contributions to the averaged spectra from the wind noise in the individual microphones. With sufficiently short averaging intervals, the array beam pattern will remain almost constant during the corresponding sweep of each focus point. This means that a deconvolution calculation can be performed for each FFT frequency line and for each averaging interval in order to enhance resolution, suppress sidelobes and scale the maps. “Beamforming and Deconvolution Calculations” on page 8 elaborates on the compensation for Doppler effects in the calculation of the PSF used for the deconvolution.

Compensation for wind was not implemented in the prototype software used for data processing. Fortunately, there was almost no wind on the day when the measurements used in this paper were taken. But the results presented in “Application to MU300 Business-jet Fly-over” on page 16 reveal some small source offsets which could probably be reduced through a wind correction to be supported in released software. The prototype software also does not support compensation for atmospheric losses. Such compensation will be needed to correctly reconstruct the source levels on the aircraft, but is not necessary to estimate the contributions from selected areas on the aircraft to the sound pressure at the array.

Overall System Architecture

Fig. 1 shows the array geometry (left) and a picture of the array deployed on the runway. The array design and the use of a frequency-dependent smooth array-shading function are inspired by [2]. However, to support quick and precise deployment on the runway, a simpler star-shaped array geometry was implemented. The full array consists of nine identical line-arrays which are joined together at a centre plate and with equal angular spacing controlled by aluminium

arcs. The 12 microphones on one line array of length 6 metres were clicked into an aluminium tube, which was rotated in such a way around its axis that the ¼ inch microphones were touching the runway. The surface geometry of the part of the runway where the array was deployed was very smooth and regular, so it could be characterized to a sufficient accuracy by just measuring a few slope parameters. Measurement of individual microphone coordinates was therefore not necessary: the vertical positions were automatically and accurately obtained from the known microphone coordinates in the horizontal plane and the runway slopes.

Fig. 1. Array geometry and picture of the array on the runway. Each microphone is clicked into position in the radial bars with the microphone tip touching the runway. "Half windscreens" can be added. The array diameter is 12 m, and there are 9 radial line arrays each with 12 microphones

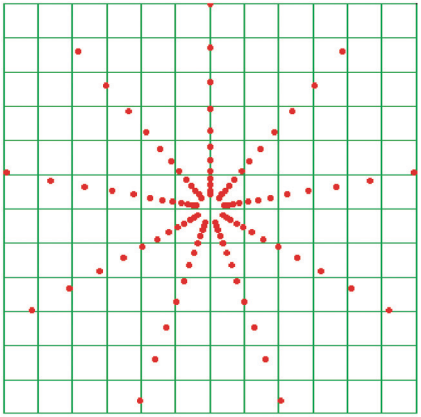

120650

Due to the turbulence-induced loss of coherence over distance, a smooth shading function was used that focuses on a central sub-array, the radius of which is inversely proportional to frequency [2]. At high frequencies only a small central part of the array is therefore used, which must then have small microphone spacing. To counteract the resolution loss at low-to-medium frequencies resulting from the high microphone density at the centre, an additional weighting factor was applied that ensured constant effective weight per unit area over the active part of the array [2]. The effective frequency-dependent shading to be applied to each microphone signal was implemented as a zero-phase FIR filter, which was applied to the signal before the beamforming calculation.

An important reason for the use of a shading function that cuts away signals from peripheral microphones at higher frequencies is to ensure that the PSF used for deconvolution will approximate the beamformer response to a point source measured under realistic conditions with air turbulence. The PSF is obtained purely from a mathematical model, so it will not be affected by air turbulence. If the PSF does not accurately model an actually measured point source response, then the deconvolution process cannot accurately estimate the underlying real source distribution that leads to the measured DAS map. The shading function must guarantee that at every frequency we use only a central part of the array that is not highly affected by air turbulence [2].

A different way of handling the problem of a limited coherence diameter would be the use of nested arrays, where different sub-arrays are used in different frequency bands [5]. An advantage of the array design and shading method chosen in this paper is the possibility of changing the shading function, and thus the active sub-array, continuously with frequency. As will be outlined below, Doppler correction must be applied in the shading filter, when that filter is used in the PSF calculation.

As the array target frequency range was from 500 Hz to 5 kHz, a sampling rate of 16384 samples/second had to be used. The microphones were Brüel & Kjær Type 4958 array microphones, and a Brüel & Kjær PULSE™ front-end was used for the acquisition. In addition to the 108 array microphone signals, an IRIG-B signal and a line camera trigger signal were also recorded. While GPS data from the aircraft would be available through file transfer only after the measurement campaign, the line camera signal provided immediate information about aircraft passage time over the camera position within the time interval of the recorded microphone signals.

Beamforming and Deconvolution Calculations

The implemented fly-over beamforming software supports two different kinds of output map on the aircraft: Pressure Contribution Density and Sound Intensity. Both quantities can be integrated over selected areas on the aircraft to obtain the contributions from these areas to the sound pressure at the array and the radiated sound power, respectively. This paper is concerned only with the first quantity.

As argued above, the estimation of the Pressure Contribution Density does not require any compensation for losses during wave propagation in the atmosphere. For the same reason, Doppler amplitude correction is not required either. The first calculation step is to apply the shading filters $W_m(\omega)$ to the measured microphone pressure signals $p_m(t)$, $m = 1, 2, \ldots, M$ being an index over the M microphones, ω

the temporal angular frequency and t the time. To achieve equal weight per area over the active central sub-array, the shading filters were defined as [2]:

$$W_m(\omega) = K(\omega)R_m^2\left\{1 - \mathrm{Erf}\left[\kappa\left(\frac{R_m}{R_{\mathrm{coh}}(\omega)} - 1\right)\right]\right\} \tag{1}$$

where R_m is the distance from microphone m to the array centre, Erf is the Error Function, κ is a factor that controls the steepness of the radial cut-off, $R_{\mathrm{coh}}(\omega)$ is the assumed frequency-dependent coherence radius (i.e., the radius of the active sub-array). Finally, $K(\omega)$ is a scaling factor ensuring that at every frequency the sum of the microphone weights equals one. The filters $W_m(\omega)$ are applied to the microphone signals as a set of FIR filters. Effectively, the microphone signals are convolved by the impulse responses $w_m(\tau)$ of the filters, providing the shaded microphone signals $\hat{p}_m(t)$:

$$\hat{p}_m(t) = (p_m \otimes w_m)(t) \tag{2}$$

For each point in the calculation mesh following the aircraft, DAS beamforming is then performed as:

$$b_j(t) = \sum_{m=1}^{M} \hat{p}_m\left(t + \frac{r_{mj}(t)}{c}\right) \tag{3}$$

$b_j(t)$ being the beamformed time signal at a focus point with index j, c the propagation speed of sound, and $r_{mj}(t)$ the distance from microphone m to the selected focus point at time t. Eq. (3) must be calculated once for each desired sample of the beamformed signal, typically with the same sampling frequency as the measured microphone signals. With the applied rather low sampling rate in the acquisition, sample interpolation had to be performed on the microphone signals to accurately take into account the delays $r_{mj}(t)/c$. Eq. (3) inherently performs a de-dopplerization providing the frequency content at the source [2].

Once the beamformed time signals have been computed, averaging of Autopower spectra (using FFT) is performed for each focus point in time intervals that correspond to selected position intervals of the aircraft, typically of 10 m

length. With a flight speed of 60 m/s, 256 samples FFT record length, 16384 samples/second sampling rate, and 66.6% record overlap, the number of averages will be around 30. For the subsequent deconvolution calculation, an averaged spectrum is considered as belonging to a fixed position – the position of the focus point at the middle of the averaging time interval.

To introduce deconvolution and derive the associated PSF in a simple way, the case of non-moving source and focus points, i.e., with $r_{mj}(t)$ equal to a constant distance r_{mj}, shall be considered first. Using $e^{j\omega t}$ as the implicit complex time factor, Eq. (3) is then easily transformed to the frequency domain:

$$B_j(\omega) = \sum_{m=1}^{M} W_m(\omega) P_m(\omega) e^{jkr_{mj}} \tag{4}$$

where B_j is the beamformed spectrum, W_m is the shading filter applied to microphone m, P_m is the spectrum measured by microphone m, and $k = \omega/c$ is the wavenumber.

Consider now a source model in terms of a set of I incoherent monopole point sources at each one of a grid of focus positions. Let $i = 1, 2, \ldots, I$ be an index over the sources and $j = 1, 2, \ldots, I$ an index over the focus point. The sound pressure at microphone m due to source i is then expressed in the following way:

$$P_{mi}(\omega) \equiv Q_i(\omega) s_{0i} \frac{e^{-jks_{mi}}}{s_{mi}} = Q_i(\omega) \frac{s_{0i}}{s_{mi}} e^{-jks_{mi}} \tag{5}$$

where Q_i is the source amplitude, s_{mi} is the distance from microphone m to source number i, and s_{0i} is the distance from the centre of the array to source number i. With this definition, Q_i is simply the amplitude of the sound pressure produced by source number i at the centre of the array, which can be seen from Eq. (5) by considering the array centre as microphone number 0. The beamformer output B_{ij} at position j due to source i is now obtained by use of Eq. (5) in Eq. (4):

$$B_{ij}(\omega) = \sum_{m=1}^{M} W_m(\omega) P_{mi}(\omega) e^{jkr_{mj}} = Q_i(\omega) \sum_{m=1}^{M} W_m(\omega) \frac{s_{0i}}{s_{mi}} e^{jk(r_{mj} - s_{mi})} \tag{6}$$

Based on Eq. (6) we define the power transfer function $H_{ij}(\omega)$ from source i to focus point j through the beamforming measurement and calculation process as follows:

$$H_{ij}(\omega) \equiv \left| \frac{B_{ij}(\omega)}{Q_i(\omega)} \right|^2 = \left| \sum_{m=1}^{M} W_m(\omega) \frac{s_{0i}}{s_{mi}} e^{jk(r_{mj} - s_{mi})} \right|^2 \tag{7}$$

Since the sources are assumed incoherent, they contribute additively to the power at focus position j, so defining the source power spectrum as $S_i \equiv \frac{1}{2}|Q_i|^2$, the total power represented by the source model at focus point j is:

$$\Pi_{\text{model},\,j}(\omega) = \sum_i H_{ij}(\omega) S_i(\omega) \tag{8}$$

Deconvolution algorithms aim at identifying the non-negative point source power values S_i of the model such that the modelled power at all focus points approximates as closely as possible the power values $\Pi_{\text{measured},\,j}$ obtained at the same points from use of the DAS beamformer Eq. (4) on the measured microphone pressure data:

$$\text{Solve} \quad \Pi_{\text{measured},\,j}(\omega) = \sum_i H_{ij}(\omega) S_i(\omega) \quad \text{with } j = 1, 2, \ldots, I, \quad S_i \geq 0 \tag{9}$$

The set of transfer functions $H_{ij}(\omega)$ from a single source position i to all focus points j constitutes the PSF for that source position, describing the response of the beamformer to that point source:

$$\mathbf{PSF}_i(\omega) \equiv \{ H_{ij}(\omega) \}_{j = 1, 2, \ldots, I} \tag{10}$$

Once Eq. (9) has been (approximately) solved by a deconvolution algorithm, the source strengths S_i represent the sound pressure power of the i^{th} model source at the array centre. The pressure contribution density is therefore obtained just by

dividing S_i by the area of the segment on the mapping plane represented by that monopole source.

Several deconvolution algorithms have been developed for use in connection with beamforming; see, for example, [7] for the DAMAS algorithm, introduced as the first one, and [8] for an overview. The DAMAS algorithm is computationally heavy, but supports arbitrary geometry of the focus/source grid, meaning that for a fly-over application an irregular area covering only the fuselage and the wings can be used [4, 5, 8]. Another advantage of DAMAS is that it can take into account the full variation of the PSF with source position *i*. Algorithms like DAMAS2 and FFT-NNLS are much faster, because they use 2D spatial FFT for the matrix-vector multiplications to be calculated during the deconvolution iteration. This, however, sets the restrictions that i) the focus/source grid must be regular rectangular, and ii) the PSF must be assumed to be shift invariant to make the right-hand side in Eq. (9) take the form of a convolution. The second requirement can be relaxed through the use of nested iterations [8]. All results of this paper have been obtained using an FFT-NNLS algorithm based on a single PSF with source position at the centre of the mapping area. No nested algorithm was used.

Having introduced the concepts related to deconvolution in connection with non-moving sources, we now return to the case of a moving source such as an aircraft. In that case, the beamforming is performed in the time domain using Eq. (3), followed by FFT and averaging in time intervals corresponding to selected position intervals of the aircraft. As a result, we obtain for each averaging interval a set of beamformed FFT Autopower spectra $\Pi_{\text{measured},\,j}$ covering all focus point indices *j*. Associating the spectra related to a specific averaging interval with the focus grid position at the middle of the averaging interval, one might as a first approximation just use the beamformed spectra in a stationary deconvolution based on Eq. (9), i.e., with the PSF calculated using Eq. (7). This would, however, not take into account the influence of Doppler shifts in the PSF calculation. The following modification was suggested and used in [4] and [5]:

$$H_{ij}(\omega) = \left| \sum_{m=1}^{M} W_m \frac{s_{0i}}{s_{mi}} e^{jkDf_{mi}(r_{mj}-s_{mi})} \right|^2 \tag{11}$$

where Df_{mi} is the Doppler frequency shift factor of the signal from source *i* at microphone *m*:

$$Df_{mi} = \frac{1}{1 + M_0 \cos(\psi_{mi})} \tag{12}$$

Here, $M_0 \equiv |\mathbf{U}|/c$ is the Mach number, $\mathbf{U}$ being the source velocity vector, and ψ_{mi} is the angle between the velocity vector $\mathbf{U}$ and a vector from microphone m to point source number i. The inclusion of the Doppler shift factor in Eq. (11) changes to wavenumber k to the wavenumber $Df_{mi}k = (Df_{mi}\omega)/c$ seen by microphone m.

During testing of the beamforming software with simulated measurements, it turned out that the shading filter needs to be taken into account when doing Doppler corrections in the PSF calculation. Based on linear approximations in the calculation of distances, when the calculation grid is near the centre of a selected averaging interval, it is shown in the Appendix that Eq. (6) should be replaced by:

$$B_{ij}(\omega) \cong \sum_{m=1}^{M} W_m(\omega Df_{mj}) \frac{s_{0i}}{s_{mi}} \frac{Df_{mj}}{Df_{mi}} e^{jkDf_{mj}(r_{mj} - s_{mi})} Q_i\left(\omega \frac{Df_{mj}}{Df_{mi}}\right) \tag{13}$$

when processing data taken near the centre of the interval. Here, Df_{mj} is the Doppler frequency shift factor at microphone m associated with a point source at focus position j. It is defined exactly as the factor for the source point i. Provided the source spectra $Q_i(\omega)$ are very flat, the Doppler correction factor on the frequency in the argument of these spectra can be neglected, and Eq. (7) and Eq. (13) then lead to the following formula for the elements $H_{ij}(\omega)$ of the PSFs:

$$H_{ij}(\omega) \equiv \left|\frac{B_{ij}(\omega)}{Q_i(\omega)}\right|^2 \cong \left|\sum_{m=1}^{M} W_m(\omega Df_{mj}) \frac{s_{0i}}{s_{mi}} \frac{Df_{mj}}{Df_{mi}} e^{jkDf_{mj}(r_{mj} - s_{mi})}\right|^2 \tag{14}$$

One very important difference between Eq. (11) and Eq. (14) is the addition of the Doppler shift factor Df_{mj} on the frequency in the calculation of the array-shading function W_m. The need for that factor comes from the fact that in the tracking DAS algorithm the shading filters are applied to the measured microphone signals, which include the Doppler shift, while the PSF is calculated in the moving system, where Doppler correction has been made. If the array-

shading functions W_m are very flat over frequency intervals of length equal to the maximum Doppler shift, the factors Df_{mj} are, of course, not needed. Another difference between Eq. (11) and Eq. (14) is that Eq. (14) has the focus point Doppler factor Df_{mj} in the exponential functions, whereas Eq. (11) uses the source point Doppler factor Df_{mi}. However, experience from simulated measurements has shown this difference to be of minor importance, since the two factors are very similar. The influence of the amplitude factor Df_{mj}/Df_{mi} is also negligible.

Accuracy of the Point Spread Function

This section will investigate the agreement between the DAS response to a moving point source and a corresponding PSF calculated using Eq. (14). The geometry of the array described in "Overall System Architecture" on page 6 was used, and the monopole point source was passing over at an altitude equal to 60 m with a speed of 60 m/s, which is representative for the real fly-over measurements to be described in "Application to MU300 Business-jet Fly-over" on page 16. A pseudorandom type of source signal, totally flat from 0 Hz to 6400 Hz, was used, consisting of 800 sine waves of equal amplitude, but with random phases. With 16384 samples/s in the simulated measurement and an FFT record length equal to 256 samples, the FFT line width became 64 Hz, so the source signal had eight frequency lines for each FFT line. FFT and averaging was performed over 10 m position intervals of the point source along the x-axis, so the averaging time was 1/6 of a second, which is comparable with the 1/8-second period length of the source signal. The FFT and averaging used a Hanning window and 66% record overlap.

For the array shading, the radius $R_{\mathrm{coh}}(\omega)$ of the active central sub-array must be specified as a function of frequency, f. Reference [2] proposed the use of a radius inversely proportional to frequency:

$$R_{\mathrm{coh}}(f) = \frac{f_{1\ \mathrm{metre}}}{f} \cdot 1\ \mathrm{m} \tag{15}$$

$f_{1\ \mathrm{metre}}$ being the frequency with 1 metre radius of the central coherent area. Based on actual measurements, a value around 4 kHz was proposed [2]. The actual measurements presented in this paper were taken on a day with almost no wind, and we have found a value of $f_{1\ \mathrm{metre}} = 6$ kHz to provide good results, so that value has also been used in the simulated measurements.

After shading, DAS beamforming was performed with a grid of 61 × 61 points with 0.25 m spacing, covering an area of 15 m × 15 m with the point source at the centre. The PSF was then calculated across the same grid of points, for a source also at the centre. Diagonal Removal was not applied.

Fig. 2. Relative average deviation between PSF and DAS over a 15 m x 15 m area centred at x = –30 m

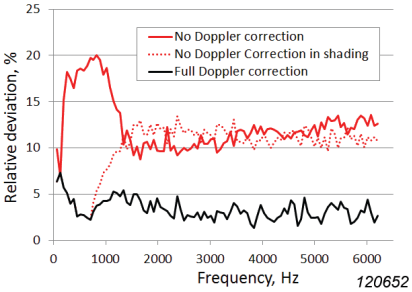

a) Shading slope factor κ = 2.0

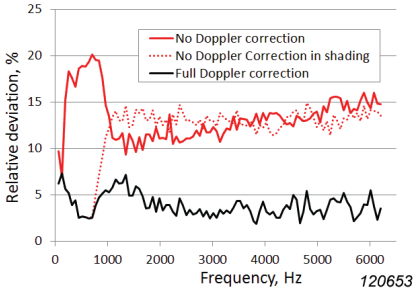

b) Shading slope factor κ = 4.0

Fig. 2 shows, as a function of frequency, the average relative deviation between the two maps calculated as:

$$\text{Relative Deviation} = \frac{\sqrt{\sum_j (H_{ij} - \Pi_{\text{measured},j})^2}}{\sqrt{\sum_j (\Pi_{\text{measured},j})^2}} \cdot 100\% \qquad (16)$$

where the PSF source position i is at the centre of the area, and $\Pi_{\text{measured},j}$ is from a simulated measurement on that source with unit amplitude. Fig. 2a shows the result for a rather smooth radial cut-off in the shading function, $\kappa = 2.0$, while in Fig. 2b a medium-steep cut-off $\kappa = 4.0$ was used. In both cases, three levels of Doppler correction were used in the calculation of the PSF. The full red curve represents the case of no Doppler correction made, meaning that the PSF was calculated from Eq. (7). For the dotted red curve Eq. (14) was used, but without the Doppler shift factor in the shading function W_m. The result is almost identical with what would be obtained using Eq. (11). The full black spectrum is obtained using Eq. (14). Clearly, use of the Doppler factor is needed in the calculation of

the shading function. The remaining error was highly dependent on the applied signal and the averaging time, and no other important influencing factors were identified. So this residual error seems to be caused by the very short averaging performed in the tracking DAS beamformer. The change in shape of the deviation spectra around 800 Hz occurs where the radial cut-off of the shading function sets in.

Fig. 3 shows the deviation achieved through use of Eq. (14) for PSF calculation at a set of x-coordinates. The deviation is seen to have approximately the same level independent of position during the simulated fly-over, when Eq. (14) is used for calculation of the PSF.

Fig. 3. Relative average deviation between PSF and DAS over a 15 m x 15 m area centred at a set of different x-coordinates. $\kappa = 4.0$

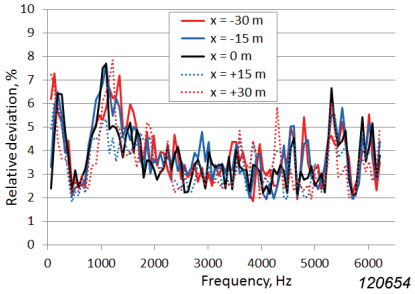

Application to MU300 Business-jet Fly-over

The system was applied as a part of a fly-over test campaign in November 2010 at Taiki Aerospace Research Field (Taiki, Hokkaido, Japan) under joint research work between JAXA and Brüel & Kjær. JAXA was conducting the test campaign, where fly-over noise source localization technologies, including their own acoustic array, were developed. Around 120 measurements were taken on an MU300 business jet from Mitsubishi Heavy Industries. Fig. 5 shows the MU300 aircraft, which has overall length and width equal to 14.8 m and 13.3 m, respectively. It has two jet engines on the body, just behind and over the wings. The nose of the aircraft is used as the reference in the position information obtained from the onboard GPS system. As indicated in Fig. 4, the centre of the global coordinate system is on the runway at the centre of the array.

The approach adopted for time-alignment of array recordings and aircraft position information from the aircraft was described in “Overall System

Fig. 4. Taiki Aerospace Research Field with indication of array position and global coordinate system

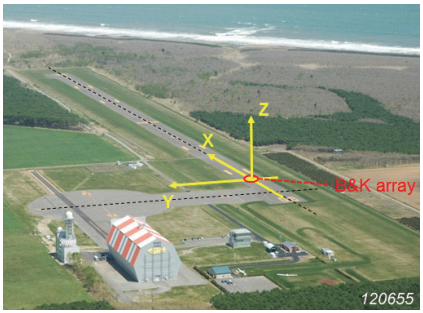

Fig. 5. Picture of the MU300 business jet

Architecture" on page 6. The data file from the on-board GPS based positioning system provided the following information (at 5 m intervals along the runway):

- Very accurate absolute time from the IRIG-B system
- Three position coordinates with accuracy between 5 cm and 30 cm
- Three speed coordinates with accuracy around 0.005 m/s
- Roll, pitch and yaw with approximate accuracy 0.005°

This information in combination with the IRIG-B signal recorded with the microphone signals was used in all data processing for accurate reconstruction of the aircraft position at every sample of the microphone signals.

Illustration of Processing Steps

The purpose of this section is just to illustrate the huge improvement in resolution and dynamic range that is achieved through the combination of shading and deconvolution. For this illustration a *level flight* was chosen with *engine idle* and the aircraft in *landing configuration*. Altitude was 59 m, and the speed was 57 m/s.

Fig. 6 shows results for the 1 kHz octave band, averaged over a 15 m interval centred where the nose of the aircraft is 5 m past the array centre, i.e., at $x = 5$ m. The resulting FFT spectra were synthesized into full octave bands. The displayed dynamic range is 20 dB, corresponding to 2 dB level difference between the colours. Fig. 6a shows the DAS map obtained without shading, meaning that resolution will be poor due to the concentration of microphones near the array centre. Use of the shading function improves resolution considerably, as seen in Fig. 6b, but it also amplifies the sidelobes due to the large microphone spacing across the outer part of the active sub-array, where each microphone is also given a large weight. Fortunately, the deconvolution process is able to significantly reduce

Fig. 6. Illustration of the improvements in resolution and dynamic range obtained through the use of shading and deconvolution. The data are from a level flight with engine idle and the aircraft in landing configuration. The display dynamic range is 20 dB, corresponding to 2 dB contour interval

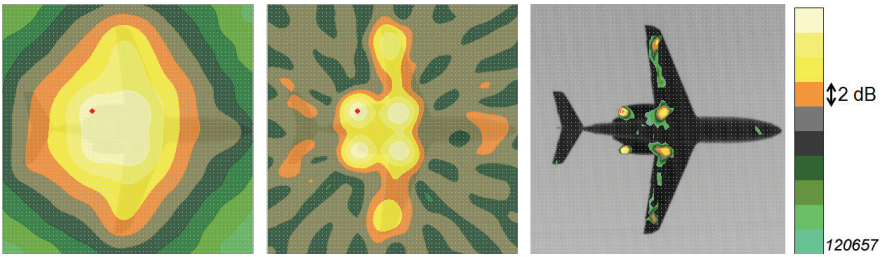

a) DAS, no shading, no diagonal removal

b) DAS, shading, no diagonal removal

c) DAS + NNLS, shading, diagonal removal

these sidelobes, as can be seen in Fig. 6c. Better sidelobe suppression could have been achieved in DAS by the use of more optimized irregular array geometries (e.g., multi-spiral), but here the focus has been on the ease of array deployment, and deconvolution seems to compensate quite well.

All maps were calculated using a 16 m × 16 m grid with 0.25 m spacing, leading to 65 × 65 = 4225 calculation points. In the following, 10 m averaging intervals will be always used. The total calculation time for seven intervals, including DAS and FFT-NNLS calculations, was approximately 5 min on a standard Dell Latitude E6420 PC.

Contour Plots of Pressure Contribution Density

The results to be presented in this section and in "Pressure Contribution Spectra at the Centre of the Array" on page 19 are all from a *level flight* at 63 m altitude, with 61 m/s speed, *engine idle*, and with the aircraft in *clean configuration*. All results were obtained using shading, diagonal removal and FFT-NNLS deconvolution based on a PSF with full Doppler correction as described in Eq. (14).

Fig. 7 contains contour plots of the pressure contribution density for the 1 kHz octave band when the nose of the aircraft is at x = –30, –10, +10 and +30 m. A 20 dB fixed display range has been used to reveal source level changes during the fly-over. At x = +10 m the engine nozzles are almost exactly over the centre of the array. The strong nozzle sources are seen to shift a bit in the x-direction as the aircraft moves past the array. This is at least partially because the engine is at a slightly higher altitude than the mapping plane, which is at the level of the aircraft nose, see Fig. 5. Based on aircraft geometry, the nozzle sources should shift

Fig. 7. Pressure contribution density plots for the 1 kHz octave at four positions during a level flight with engine idle and the aircraft in clean configuration. The averaging intervals were 10 m long and centred at the listed positions. The 20 dB colour scale from Fig. 6 is reused. Threshold is constant across the four maps with full dynamic range used at x = +10 m, where the engine nozzles are exactly over the array centre

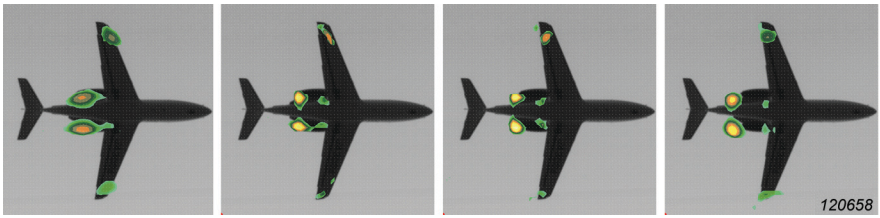

a) x = –30 m b) x = –10 m c) x = +10 m d) x = +30 m

approximately 1/3 of the engine length due to that phenomenon when the aircraft moves from x = –30 m to x = +30 m. The two weaker sources in front of the nozzles are probably the intakes, which are only partially visible from the array because of the wings. Close to the wing tips, two more significant sources are seen in this 1 kHz octave band. Probably these sources are the openings of two drain tubes or small holes and gaps. The narrowband spectral results to be presented in "Pressure Contribution Spectra at the Centre of the Array" on page 19 show that these two sources are narrow-banded and concentrated near 1 kHz.

Fig. 8 contains contour plots similar to those of Fig. 7, but with the nose of the aircraft at x = 0 m and covering the octave bands from 500 Hz to 4 kHz. Clearly, the two sources some small distance from the wing tips exist only within the 1 kHz octave band. The 500 Hz octave includes frequencies well below 500 Hz, where the array is too small to make deconvolution work effectively, so here resolution is poor. Notice that the system provides almost constant resolution across a fairly wide frequency range. This is also true for the DAS maps, i.e., without deconvolution, the explanation being that the diameter of the active sub-array is inversely proportional to frequency above 1 kHz.

Pressure Contribution Spectra at the Centre of the Array

As mentioned in "Contour Plots of Pressure Contribution Density" on page 18, the pressure contribution density maps – such as those in Fig. 7 – can be area integrated to give estimates of the contributions from selected areas to the sound pressure at the centre of the array. As a reference for these contributions, and for validation purposes, it is desirable to compare them with the pressure measured directly at the array. Since there was no microphone at the array centre, the

Fig. 8. Octave band pressure contribution density maps for the averaging interval at x = 0. Again, the 20 dB colour scale from Fig. 6 is reused. For each map the threshold is adjusted to show a 20 dB range

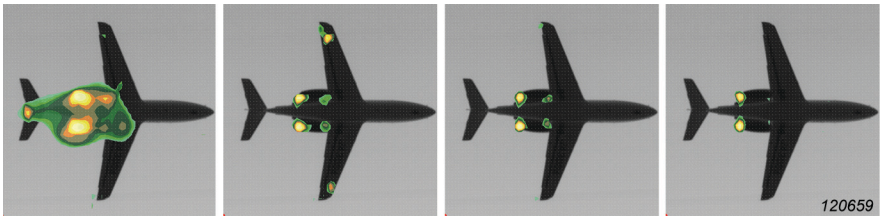

a) 500 Hz octave b) 1 kHz octave c) 2 kHz octave d) 4 kHz octave

average pressure power across all microphones was used. The directly measured spectra, however, contain Doppler shifts, whereas the area-integrated spectra are based on maps of de-dopplerized data. To compare the spectral contents, the Doppler shift status must be brought into line for the two spectra. Since it is natural to have the Doppler shift included when dealing with the noise at the array, a choice was made to "re-dopplerize" the pressure contribution density maps on the aircraft. So this was actually done also for the maps in Fig. 7 and Fig. 8.

Fig. 9. Measured average pressure spectrum compared with pressure contributions calculated by integrating over the full mapping area seen in Fig. 7d

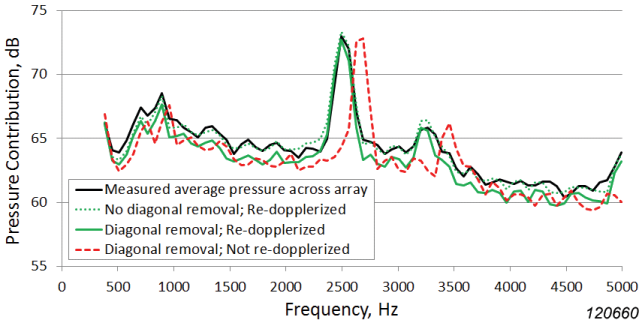

The full black curve in Fig. 9 represents the directly measured array pressure spectrum based on FFTs with 256 samples record length, Hanning window, and averaging over a time interval corresponding to that used at the aircraft, but delayed with the sound propagation time from the aircraft to the array. The three pressure contribution spectra in the same figure were integrated over the full

mapping area for the averaging interval at x = +30 m, also represented in Fig. 7d. As expected, the re-dopplerization shifts the spectral peaks in the contribution spectra downwards to match very well with the peaks in the measured array pressure spectrum. Without diagonal removal, the level of the calculated contribution spectrum matches very well with the measured array pressure. Diagonal removal leads to a small under-estimation amounting to approximately 1 dB, part of which is flow noise in the individual microphones.

In the derivation of the PSF in Eq. (14) we had to assume a flat spectrum to proceed from Eq. (13). Clearly, the spectrum in Fig. 9 is not flat around the narrow peak at 2.5 kHz. Eq. (14) was used anyway across the full frequency range, and the spectral peaks seem well reproduced. But to ensure accurate handling of Doppler effects around sharp spectral peaks (tones) in deconvolution, a special handling should be implemented modelling the energy flow between frequency lines [4]. This becomes an important issue, if the level difference between a peak and the surrounding broadband spectrum approaches or even exceeds the dynamic range (sidelobe suppression) of the array with DAS beamforming. This is not the case here, but close.

By integrating the pressure contribution density over only partial areas, one can estimate the contribution from these areas to the sound pressure at the array. Fig. 10 shows a set of sub-areas to be considered beyond the full mapping area: i) the engine nozzles; ii) the central area, covering engine intake, wheel wells, and the inner part of the wings; iii) the outer part, approximately 1/3 of both wings. The colours of the areas will be re-used in the contribution spectra.

Fig. 11 contains the contribution spectra for the same aircraft positions as represented by the contour maps in Fig. 7. In the present *clean* configuration of the aircraft, the engine nozzles are seen to have by far the dominating noise contribution, even though the engine is in idle condition. A small exception is a narrow frequency band near 1 kHz, where the sources near the wing tips are dominant. Except for very few exceptions, the full area contribution is within 1 dB from the measured average sound pressure over the array. Part of this difference is due to flow noise in the individual microphones. So the underestimation on the full-area contribution due to the use of diagonal removal is very small, but may cause low-level secondary sources in Fig. 7 and Fig. 8 to become invisible. The 30 dB dynamic range shown in the spectra of Fig. 11 is probably a bit too large to say that all visible details are “real”.

Fig. 10. Sub-areas used for integration of pressure contribution. The sources at the inner front edge of the wings are probably two fins

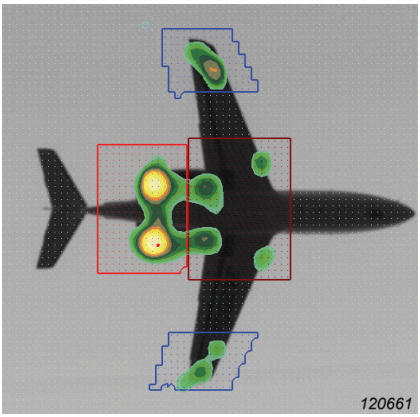

Fig. 11. Pressure contributions from the areas of Fig. 10 to the sound pressure at the array centre

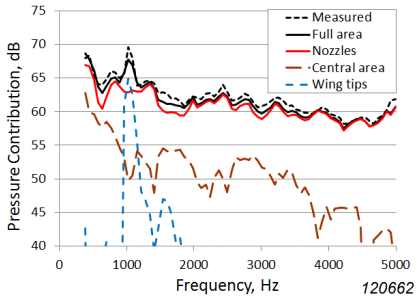

a) x = –30 m

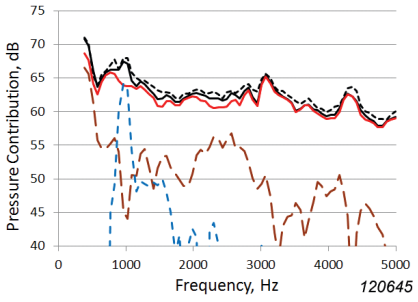

b) x = –10 m

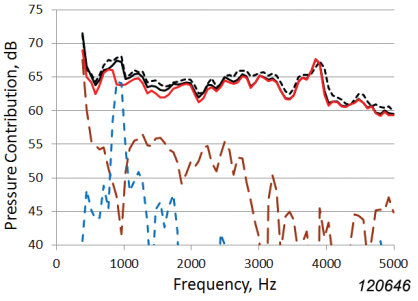

c) x = +10 m

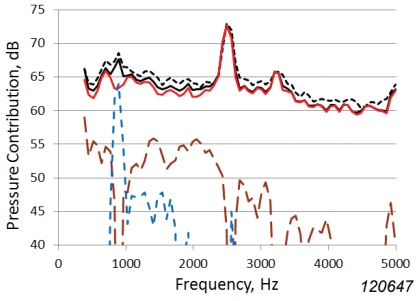

d) x = +30 m

Conclusion

The paper has described a system and a methodology for performing high-resolution fly-over beamforming using an array designed for fast and precise deployment on a runway. Due to this requirement, a rather simple array geometry not optimized for best sidelobe suppression was used. Our hope was that the use of deconvolution could compensate for that. The system was designed to cover the frequency range from 500 Hz to 5 kHz, and it proved to provide very good resolution and dynamic range across these frequencies, except perhaps just around 500 Hz. Results have been presented in the paper from a couple of measurements out of approximately 120 recordings taken on an MU300 business jet at Taiki Aerospace Research Field, Taiki, Hokkaido, Japan, in November 2010. The results are very encouraging.

A special focus has been on the use of an array-shading function that changes continuously with frequency, and in particular on the implications of that in connection with deconvolution. It was shown that Doppler shifts have to be taken into account in the use of the shading function in connection with calculation of the Point Spread Function used for deconvolution.

Appendix

This appendix presents a derivation of Eq. (13). We consider an arbitrarily selected averaging interval, and we choose also arbitrarily a single model point source with index *i*. For convenience we measure time relative to the centre of the selected averaging interval.

The first problem is to derive a linear approximation for the time t_m where the source signal radiated at time t_s reaches microphone *m*, valid for $|t_s| << 1$. To do that, the distance from point source *i* to microphone *m* is approximated as:

$$s_{mi}(t_s) \cong s_{mi} + \cos(\psi_{mi}) U t_s \qquad \text{for } |t_s| << 1 \tag{17}$$

where $U \equiv |\mathbf{U}|$ is the aircraft speed, and ψ_{mi} is the angle between the velocity vector **U** and a vector from microphone *m* to the point source, both at the centre of the averaging interval. In the same way we get for the distance from focus point *j* to the microphone:

$$r_{mj}(t) \cong r_{mj} + \cos(\psi_{mj}) U t \qquad \text{for } |t| << 1 \tag{18}$$

The signal radiated at time t_s arrives at microphone *m* at time t_m given as:

$$t_m = t_s + \frac{s_{mi}(t_s)}{c} \tag{19}$$

Using Eq. (17) and the expression in Eq. (12) for the Doppler shift factor, we can rewrite Eq. (19) as:

$$t_m \cong \frac{s_{mi}}{c} + \frac{t_s}{Df_{mi}} \tag{20}$$

This equation is easily solved for t_s with the result:

$$t_s \cong Df_{mi} \cdot \left(t_m - \frac{s_{mi}}{c} \right) \tag{21}$$

which is then valid for $|t_m - s_{mi}/c| << 1$.

For the microphone signals from point source i we need an expression equivalent with Eq. (5), just in the time domain and for the moving source. As argued in "Beamforming and Deconvolution Calculations" on page 8, the Doppler amplitude factor can be neglected, when estimating Pressure Contributions. Doing that, the microphone pressure gets the following simple form [2]:

$$p_{mi}\left(t_s + \frac{s_{mi}(t_s)}{c}\right) = s_{0i}\frac{q_i(t_s)}{s_{mi}(t_s)} \tag{22}$$

containing the propagation delay $s_{mi}(t_s)/c$ and the inverse distance decay in connection with the source signal q_i. In Eq. (22) we approximate the time-varying inverse distance decay by its value for $t_s = 0$, and we use the delay approximation of Eq. (21):

$$p_{mi}(t_m) \cong \frac{s_{0i}}{s_{mi}} q_i\left(Df_{mi} \cdot \left(t_m - \frac{s_{mi}}{c}\right)\right) \qquad \text{for} \quad \left|t_m - \frac{s_{mi}}{c}\right| << 1 \tag{23}$$

The first step in the DAS calculation is application of the individual shading filters to the microphone signals. In the time domain this can be expressed as convolution with the impulse responses $w_m(\tau)$ of these filters, see Eq. (2):

$$\begin{aligned} \hat{p}_{mi}(t_m) &= (p_{mi} \otimes w_m)(t_m) = \int_{-\infty}^{\infty} p_{mi}(\tau) w_m(t_m - \tau) d\tau \\ &\cong \frac{s_{0i}}{s_{mi}} \int_{-\infty}^{\infty} q_i\left(Df_{mi} \cdot \left(\tau - \frac{s_{mi}}{c}\right)\right) w_m(t_m - \tau) d\tau \end{aligned} \tag{24}$$

Here the approximation of Eq. (23) has been inserted. An apparent conflict in this context is the integral going from $-\infty$ to $+\infty$ while at the same time we use an approximation valid for only small values of the integration variable. Both here and in the later Fourier integrals we have to think of using windowed source signals, meaning that the integrals will have contributions only from time segments close to time zero.

The shaded microphone signals are now used in DAS beamforming as expressed in Eq. (3):

$$b_{ij}(t) = \sum_{m=1}^{M} \hat{p}_{mi}\left(t + \frac{r_{mj}(t)}{c}\right) \tag{25}$$

To proceed, we need to use the linear approximation of Eq. (18) for the distances $r_{mj}(t)$ between microphones and focus points. As a result we obtain an approximation similar to the one in Eq. (20):

$$t + \frac{r_{mj}(t)}{c} \cong \frac{r_{mj}}{c} + \frac{t}{Df_{mj}} \qquad \text{for } |t| << 1 \tag{26}$$

Use of Eqs. (26) and (24) in Eq. (25) leads to:

$$\begin{aligned} b_{ij}(t) &= \sum_{m=1}^{M} \hat{p}_{mi}\left(t + \frac{r_{mj}(t)}{c}\right) \cong \sum_{m=1}^{M} \hat{p}_{mi}\left(\frac{r_{mj}}{c} + \frac{t}{Df_{mj}}\right) \\ &\cong \sum_{m=1}^{M} \frac{s_{0i}}{s_{mi}} \int_{-\infty}^{\infty} q_i\left(Df_{mi} \cdot \left(\tau - \frac{s_{mi}}{c}\right)\right) w_m\left(\frac{r_{mj}}{c} + \frac{t}{Df_{mj}} - \tau\right) d\tau \end{aligned} \tag{27}$$

The final step to obtain the frequency domain response $B_{ij}(\omega)$ is to Fourier transform the signal $b_{ij}(t)$. To do that we notice first that in Eq. (27) the time variable t occurs only in the argument of the shading impulse response function w_m. The argument of w_m has the form of a linear function of t. To work out the Fourier integral of $b_{ij}(t)$ we therefore need the following formula:

$$\int_{-\infty}^{\infty} w(at+b) e^{-j\alpha\omega t} dt = a^{-1} e^{j\omega\alpha b/a} W\left(\frac{\alpha}{a}\omega\right) \tag{28}$$

with $\alpha = 1$, $a = (Df_{mj})^{-1}$, and $b = (r_{mj}/c) - \tau$. W is the Fourier transform of w. Eq. (28) can be easily verified by substituting a new variable for $(at+b)$ in the integral. From use of Eq. (28) in Eq. (27) we get:

$$
\begin{aligned}
B_{ij}(\omega) &\equiv \int_{-\infty}^{\infty} b_{ij}(t) e^{-j\omega t} dt \qquad (29)\\
&\cong \sum_{m=1}^{M} \frac{s_{0i}}{s_{mi}} \int_{-\infty}^{\infty} q_i\left(Df_{mi} \cdot \left(\tau - \frac{s_{mi}}{c}\right)\right) Df_{mj} e^{jDf_{mj}\omega\left(\frac{r_{mj}}{c} - \tau\right)} W_m(Df_{mj}\omega) d\tau \\
&= \sum_{m=1}^{M} W_m(Df_{mi}\omega) \frac{s_{0i}}{s_{mi}} Df_{mj} e^{jDf_{mj}\omega\frac{r_{mj}}{c}} \int_{-\infty}^{\infty} q_i\left(Df_{mi} \cdot \left(\tau - \frac{s_{mi}}{c}\right)\right) e^{-jDf_{mj}\omega\tau} d\tau
\end{aligned}
$$

where the factors are just re-arranged in the last line. The remaining integral in Eq. (29) has also the form of Eq. (28), only with $\alpha = Df_{mj}$, $a = Df_{mi}$, and $b = -Df_{mi}s_{mi}/c$. Use of Eq. (28) with these parameter values in Eq. (29) leads to:

$$
\begin{aligned}
B_{ij}(\omega) &\cong \sum_{m=1}^{M} W_m(Df_{mj}\omega) \frac{s_{0i}}{s_{mi}} Df_{mj} e^{jDf_{mj}\omega\frac{r_{mj}}{c}} \frac{1}{Df_{mi}} e^{j\omega\left(-Df_{mj}\frac{s_{mi}}{c}\right)} Q_i\left(\frac{Df_{mj}}{Df_{mi}}\omega\right) \\
&= \sum_{m=1}^{M} W_m(Df_{mj}\omega) \frac{s_{0i}}{s_{mi}} \frac{Df_{mj}}{Df_{mi}} e^{jDf_{mj}k(r_{mj} - s_{mi})} Q_i\left(\frac{Df_{mj}}{Df_{mi}}\omega\right) \qquad (30)
\end{aligned}
$$

which is the expression given in Eq. (13). Q.E.D.

Acknowledgments

The authors would like to thank Diamond Air Service Incorporation for their support in conducting the fly-over tests.

References

[1] Michel, U., Barsikow, B., Helbig, J., Hellmig, M., and Schüttpelz, M., "Flyover Noise Measurements on Landing Aircraft with a Microphone Array," *AIAA Paper 98-2336*.

[2] Sijtsma, P. and Stoker, R., "Determination of Absolute Contributions of Aircraft Noise Components Using Fly-over Array Measurements," *AIAA Paper 2004-2958*.

[3] Guérin, S., Weckmüller, C., and Michel, U., "Beamforming and Deconvolution for Aerodynamic Sound Sources in Motion," *Berlin Beamforming Conference (BeBeC) 2006, Paper BeBeC-2006-16*.

[4] Guérin, S., and Weckmüller, C., "Frequency Domain Reconstruction of the Point-spread Function for Moving Sources," *Berlin Beamforming Conference (BeBeC) 2008, Paper BeBeC-2008-14*.

[5] Guérin, S. and Siller, H., "A Hybrid Time-Frequency Approach for the Noise Localization Analysis of Aircraft Fly-overs," *AIAA Paper 2008-2955*.

[6] Siller, H., Drescher, M., Saueressig, G., and Lange, R., "Fly-over Source Localization on a Boeing 747-400," *Berlin Beamforming Conference (BeBeC) 2010, Paper BeBeC-2010-13*.

[7] Brooks, T.F., Humphreys, W.M., "A Deconvolution Approach for the Mapping of Acoustic Sources (DAMAS) Determined from Phased Microphone Arrays," *AIAA Paper 2004-2954*.

[8] Ehrenfried, K. and Koop, L., "A comparison of iterative deconvolution algorithms for the mapping of acoustic sources," *AIAA Paper 2006-2711*.

Clustering Approaches to Automatic Modal Parameter Estimation*

S. Chauhan and D. Tcherniak

Abstract

Most modal parameter estimation techniques utilize Stabilization/Consistency Diagrams as a tool for distinguishing between physical system modes and mathematical modes. However, this process results in giving several estimates of the same mode and the task of choosing one estimate over the others is left to the user. This task is highly judgmental, with user expertise playing a big role as to which estimate is selected, and can be very tedious, especially in situations when the data is difficult to analyze (low signal-to-noise ratio, closely spaced modes, heavily damped modes, etc.). One of the ways to get around this issue is to incorporate smart selection of estimates in the algorithm itself, so as to avoid the user interaction which, as stated previously, can be very subjective.

In this paper, two clustering-based approaches are suggested for the purpose of automatic mode selection. These methods build upon the existing Stabilization Diagram tool; differing in the manner in which the stabilization diagram is constructed and clusters are being formed. Both approaches utilize a Euclidian distance-based approach to automatically select the best estimate.

Résumé

La plupart des méthodes d'estimation des paramètres modaux font intervenir des diagrammes de stabilisation/cohérence, cet outil servant à faire la distinction entre modes de systèmes réels et modes mathématiques. Toutefois, ces processus résultent en plusieurs estimations d'un même mode, laissant à l'opérateur la responsabilité de choisir l'une d'entre elles. C'est une tâche souvent très fastidieuse, surtout lorsque les données sont très difficiles à analyser (faible rapport signal/bruit, modes peu espacés, modes très amortis, etc.) et qui fait

* First published in Proc. 27th Conference and Exposition on Structural Dynamics 2009 (IMAC XXVII)

fortement appel à son jugement et à son expérience. Un des moyens de contourner cette difficulté est d'incorporer à l'algorithme une sélection judicieuse d'estimations afin d'éviter de trop faire appel à la subjectivité de l'opérateur.

Cet article suggère deux approches sectorielles pour la sélection automatique des modes. Ces méthodes s'appuient sur l'outil diagramme de stabilisation existant, mais diffèrent dans la manière de construire ce dernier et de grouper les diagrammes. Toutes deux font appel à une approche basée sur la distance euclidienne pour sélectionner automatiquement la meilleure estimation.

Zusammenfassung

Die meisten Techniken zur Modalparameterbestimmung verwenden Stabilitäts/ Konsistenz-Diagramme als Werkzeug zur Unterscheidung zwischen physikalischen Systemmoden und mathematischen Moden. Dieser Prozess ergibt jedoch mehrere Abschätzungen für dieselbe Mode und die Aufgabe, eine davon auszuwählen und den anderen vorzuziehen, wird dem Anwender überlassen. Es handelt sich weitgehend um eine Ermessensfrage, wobei die Sachkenntnis des Anwenders beim Auswählen der Abschätzung eine große Rolle spielt, und die Aufgabe kann schwerfallen, besonders bei Daten, die schwierig zu analysieren sind (geringer Signal-Rauschabstand, dicht benachbarte Moden, stark gedämpfte Moden usw.). Eine Möglichkeit zur Umgehung dieses Problems besteht darin, eine intelligente Auswahl in den Algorithmus einzubauen, um die Benutzerinteraktion zu vermeiden, die wie erwähnt sehr subjektiv sein kann.

In diesem Artikel werden zwei auf Clustering basierte Ansätze für eine automatische Modenauswahl vorgeschlagen. Diese Methoden bauen auf dem vorhandenen Stabilitäts-Diagramm auf und unterscheiden sich darin, auf welche Weise das Stabilitäts-Diagramm konstruiert wird und Cluster gebildet werden. Beide Ansätze verwenden eine euklidische abstandsbasierte Methode, um automatisch die beste Abschätzung auszuwählen.

Nomenclature

ω	Frequency
$H(*)$	Frequency Response Function Matrix
$h(t)$	Impulse Response Function

N_{ref}	Number of input references
N_o	Number of output responses
m	Model order
$[\alpha]$	Denominator matrix polynomial coefficient
$[\beta]$	Numerator matrix polynomial coefficient
ERA	Eigensystem Realization Algorithm
UMPA	Unified Matrix Polynomial Approach
EMA	Experimental Modal Analysis
OMA	Operational Modal Analysis

Introduction

The Stabilization Diagram (or Consistency Diagram) is an important tool often utilized by the user for obtaining correct modal parameters. Most modal parameter estimation algorithms use this tool for distinguishing physical system modes from mathematical or computational modes. A stabilization diagram involves tracking of the modal parameters as a function of increasing model order (or change in data subsets, modal parameter estimation algorithms, etc.).

Once the stabilization diagram is prepared, the user is left with the task of choosing one estimate (of a mode) amongst the many estimates obtained at various iterations (as a function of model order or different solution set or even different parameter estimation method). This final step often poses the question "Which estimate should I choose?" The need to facilitate this process and avoid the uncertainty involved in this process of selecting an estimate based on user judgment has resulted in researchers working on approaches to automate the process of mode selection. There have been two common approaches to this; the first being a Logical Rules based approach and the second utilizing data-clustering techniques, which have been traditionally popular in fields such as pattern recognition, machine learning, data mining and bioinformatics.

In general, there are two issues that analysts face while dealing with modal parameter estimation. The first issue involves separating physical modes from computational modes and the second involves choosing an estimate, amongst several others, that best represents a mode. These also form the core of any technique that tries to automate the modal parameter estimation procedure. Pappa, James, et al., proposed a four-step logical rule based approach to automatic mode selection [1]. This approach utilized modal parameter estimation using ERA in the first step. The poles obtained are then passed through a threshold step that

eliminates the mathematical modes. Once modal parameters from the first iteration are identified and filtered using the previously mentioned steps, a logical rules based engine is used to judge whether the estimate from the next iteration is that of a new mode or an already existing one. If it turns out to be yet another estimate of an already existing mode from the previous iteration, it is found whether it is a better estimate than the already existing one (in which case it replaces the current estimate) or not. Here, it is important to note that this approach does not compare a mode in an iteration only to those from the previous iteration, as in the traditional stabilization diagram approach, but compares it with the best mode amongst those found in all previous iterations. The algorithm continues until all the iterations are completed. This approach uses a consistent-mode indicator (CMI) [2] as a measure of selecting the better of the two estimates. This approach was later improved to include the Genetic Algorithm based supervisor that required initial estimates of the modes to be searched [3]. It also included a dynamic fitness function to capture the modes that were not provided as initial estimates to be searched but might still exist as true modes of the structure.

A similar rule based approach was employed in [4]. This approach also utilizes, amongst other measures, tolerances in estimates of frequency, damping and modal vector to check whether or not a mode is stable with respect to that in the previous iteration. An important point worth noticing in this approach in comparison to the approach that Pappa, James, et al., suggested is that the estimate is only compared with modes obtained in the previous iteration. Further, MAC between the modal vectors is not used as a criterion for stability of modes but as a criterion to distinguish between double or closely spaced modes. In this manner, several clusters or groups of modes are obtained after all the iterations, with each cluster containing various estimates of the same mode. Finally, one mode in each cluster is selected as a best mode representing that cluster, the selection procedure being based on damping ratio.

In [4, 5], a methodology based on energy analysis of the modes is proposed to distinguish between system modes and spurious non-physical modes. It utilizes techniques such as model reduction, balanced truncation and pole/zero cancellation to assess the overall influence of removing a mode; true modes influencing the model greatly, spurious modes having minimal effect.

There have also been attempts to use classical clustering techniques for the purpose of automatic mode selection. These include utilizing techniques like Fuzzy C-Means Clustering, Support Vector Machine, etc. A Maximum Likelihood estimator based procedure that employs a similar multistage rule based approach

was suggested in [6]. In [7], this approach is complimented with Fuzzy Clustering, according to which the modes are classified into physical and computational modes. It is suggested in [8] that this methodology can also be used for structural health monitoring purposes.

Unlike the above approaches to utilize Fuzzy clustering to classify a mode as physical or computational, in [9] Fuzzy clustering is used not only to classify a mode as physical or computational, but also to find the final system modes. However, Fuzzy C-Means Clustering requires that the number of clusters (or in other words modes) is known beforehand. It also requires initial guesses of the cluster centres. In this work, a Genetic Algorithm based methodology was also suggested that can be used to make initial guesses about cluster centres.

In a recent paper, Carden and Brownjohn used a similar Fuzzy Clustering technique for structural health monitoring [10]. Instead of forming clusters based on frequency and damping estimates, they formed clusters based on real and imaginary parts of the obtained poles. The main purpose of this study was not automatic mode selection but structural health monitoring. The technique was applied to the Z24 bridge and Republic Plaza Office tower, a high rise building in Singapore.

In addition to the methods discussed above, some other approaches utilizing clustering techniques for automatic mode selection and better understanding of the stability diagram are found in the literature. Goethals, Vanluyten, et al., [11] used a K-Means clustering technique along with a self-learning classification algorithm, Least Squares Support Vector Machines, for separating spurious poles and real poles. This approach requires a training set for the Support Vector machine which is obtained by utilizing the clustering technique in the first stage implemented along with some rules/criteria.

One thing common to various approaches listed previously in this section is that the process of automatically selecting the modal parameters starts once the parameter estimation algorithm has provided the modes. The automation process is restricted to the task of filtering physical system modes and computational modes and selecting one out of many estimates of a single mode. It should be noted that it is very possible that this process might still not identify all the modes in the given frequency range. This is due to the fact that the performance of a modal parameter estimation algorithm depends considerably on several factors including the chosen frequency range, the choice of inputs selected as references and, most importantly, the choice of parameter estimation algorithm itself. Thus, the task of choosing an algorithm and setting its initial parameters (frequency

range of interest, number and choice of references, etc.) still hold the key to good results and require intelligent selection. In this manner, performance of automatic mode selection is also influenced by these factors.

The next section presents the conceptual background to the two approaches to automatic mode selection suggested in this paper. One of these approaches, named Best Mode based approach, presents a new way of constructing the stability diagram that is more informative in comparison with the traditional approach of constructing the stability diagram. Theoretical background is followed by results of studies conducted on an analytical rotor dataset in the third section where the performance of the two approaches is evaluated. The fact that these approaches result in formation of clusters having several estimates of the same mode also provides a means to calculate useful statistical data about the estimated modes. Finally, conclusions are made and the scope for future research is presented.

Theoretical Background

Historically, the concept of stability was applied to high-order algorithms like Least Squares Complex Exponential (LSCE) [12], Polyreference Time Domain (PTD) [13, 14], Rational Fraction Polynomial (RFP) [15], etc. This can be understood through Unified Matrix Polynomial Approach (UMPA) [16 – 18] which is a mathematical concept that helps in understanding various modal parameter estimation algorithms by developing these algorithms from a common framework. UMPA based equations for high-order algorithms in the time and frequency domains are given as:

High-order time domain

$$[[\alpha_1][\alpha_2]\ldots[\alpha_m]]_{N_{ref}\times mN_{ref}}\begin{bmatrix}[h(t_{i+1})]\\ [h(t_{i+2})]\\ \ldots\\ [h(t_{i+m})]\end{bmatrix}_{mN_{ref}\times N_o} = -[h(t_{i+0})]_{N_{ref}\times N_o} \quad (1)$$

High-order frequency domain

$$[[\alpha_1][\alpha_2]\ldots[\alpha_m][\beta_1][\beta_2]\ldots[\beta_n]]_{N_{ref}\times mN_{ref}+(n+1)N_o}\begin{bmatrix}(j\omega_i)^1[H(\omega_i)]\\(j\omega_i)^2[H(\omega_i)]\\\cdots\\(j\omega_i)^m[H(\omega_i)]\\-(j\omega_i)^1[I]\\-(j\omega_i)^2[I]\\\cdots\\-(j\omega_i)^n[I]\end{bmatrix}_{mN_{ref}+(n+1)N_o\times N_o}$$

$$= -(j\omega_i)^0[H(\omega_i)]_{N_{ref}\times N_o} \tag{2}$$

N_{ref} and N_o refer to the number of inputs (or number of reference outputs in the case of OMA) and the number of outputs. m refers to the model order and the number of roots of the equation (or poles) is $m \times N_{ref}$, out of which $2N$ are true modes of the system and the rest are non-physical or computational modes (in general $m \times N_{ref} >> 2N$). The stabilization diagram involved tracking the estimates of modal frequency, damping and mode shapes as a function of increasing model order m. Stability is generally defined in terms of tolerance percentage set for each of the three parameters: frequency, damping and mode shape. This approach is well documented and details can be obtained in [18, 28].

It should be noted that in equations (1) and (2), it is the $[\alpha_0]$ coefficient (or the lower order coefficient) that has been normalized. Similar equations can be formed by choosing different coefficient normalization. This forms yet another way of looking at the stability diagram where instead of varying the order, one can vary the coefficient being normalized (for a fixed order) and then track the stability of obtained modes as a function of coefficients [19].

As stated earlier, the concept of stabilization is not just restricted to high-order algorithms but can also be extended to other algorithms. In [20], this concept of stability was extended to other parameter estimation algorithms, in which case a diagram similar to the stability diagram, called the Consistency Diagram, is drawn. This approach is commonly applied to lower-order algorithms (Eigensystem Realization Algorithm (ERA) [21, 22], Ibrahim Time Domain (ITD) [23, 24], Polyreference Frequency Domain (PFD) [25-27]).

In a recent paper, Phillips and Allemang [28] provide several methods for obtaining clear stabilization/consistency diagrams. These methods include the utilization of normal mode criteria, using long vector comparison, both high- and low-order coefficient normalization, different frequency normalization, etc., and it is shown that effective use of these methods can greatly help in making the stabilization/consistency diagram a better tool.

*Fig. 1. A typical stability diagram: + New Mode,× Stable Frequency, * Stable Frequency and Damping, ∇ Stable Frequency and Vector, ◊ Stable Mode with Frequency, Damping and Vector all stable*

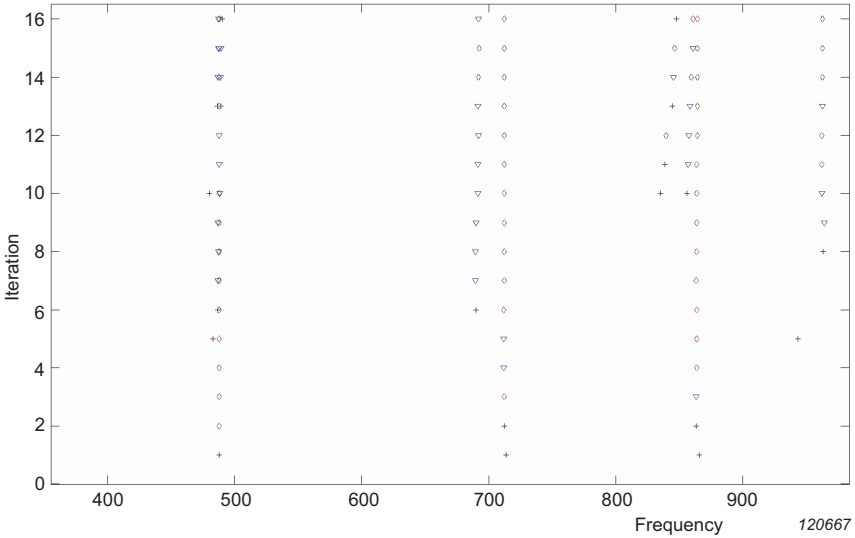

A typical stabilization diagram is shown in Fig. 1 where stabilized poles are represented by ◊. This means that if a pole stabilizes, within the user-specified tolerances of frequency, damping and vector, with respect to a mode in the previous iteration, it is represented by ◊. It should be noted that comparing a mode in an iteration to that in the previous iteration is the most common way of constructing the stability diagram. In this manner several estimates of a mode are estimated corresponding to a solution performed at various iterations (for example, in Fig. 1, 12 estimates of the mode around 720 Hz are found that are classified as stable). The task of choosing one of these twelve estimates is left to the user and, as mentioned before, this can be very tedious in cases where the user

is inexperienced, the data quality is not very good, or the structure is complex with closely coupled modes, heavily damped modes, etc. This creates a need for automating this selection process, thus avoiding user judgment by formulating a more reliable and intelligent process.

From the literature review provided in the previous section, it is apparent that various approaches towards automating this procedure involve forming of groups or clusters of valid poles (true modes of the system) obtained after the application of the modal parameter estimation technique, with each cluster representing a different mode and containing several estimates of the same mode. This procedure normally involves a logical rules based approach which is often coupled with the use of clustering algorithms like Fuzzy C-Means, K-Means, etc., to form and validate a cluster and select one estimate in a cluster as the best estimate of that particular mode.

The approaches presented in this paper are based on the fundamentals of good selection of rules and clustering technique in order to achieve the ultimate goal of automatic mode selection. For the purpose of this study, modal parameter estimation based on varying model order (suitable for high-order algorithms like PTD, RFP, etc.) is considered. It should however be noted that this procedure is extensible to other cases as well (different solution set, varying coefficient normalization, etc.). Further, in this paper only traditional FRF based experimental modal analysis studies are conducted to illustrate these techniques. However, these are equally adaptable to Operational Modal Analysis (OMA) as well.

First Approach (Traditional Stability Diagram Based)

Comparing modes from the current iteration to those in the previous iteration is a common approach to developing a stability diagram. Since this approach to automatic mode selection is based on comparing modes to those in the previous iteration only (as is the most common practice), it is referred to as Traditional Stability Diagram based approach.

Assume that a total of N iterations of modal parameter estimation are performed. At each iteration, different numbers of poles (equal to $m \times N_{ref}$, m being the model order and N_{ref} the number of references) are obtained as model order m is varied. Out of these poles, some are true system modes and others are computational modes that are to be filtered. The approach is summarised as:

1) Select a mode in $i + 1^{th}$ iteration and perform a stability test for this mode by comparing it with modes from i^{th} iteration.
2) The stability test may include several criteria like frequency, damping, mode shape tolerances, modal phase colinearity, modal phase deviation,

maximum and minimum criteria, presence of conjugate poles, positive damping, etc.

3) If the mode passes the stability criterion, it is either assigned to an already existing cluster having other estimates of the same mode or a new cluster is initiated if this is the first stable estimate of a mode.
4) The procedure is repeated for all the modes obtained in i+1th iteration, by comparing them to the modes obtained in the previous iteration (i^{th} iteration), before moving to the next iteration.
5) Steps 1 – 4 are repeated for all the iterations.
6) At the conclusion of step 5, clusters of various modes have been formed. These clusters are passed through a filtering stage to filter out those clusters that do not contain a sufficient number of estimates. This is yet another rule integrated in the process.
7) Finally, for every cluster, an estimate is selected as the best estimate representing that cluster, based on the calculation of a Euclidian distance measure. This best estimate is also the automatically selected mode.

The process flowchart is illustrated in Fig. 2.

Fig. 2. Flowchart for Traditional Stability Diagram based approach

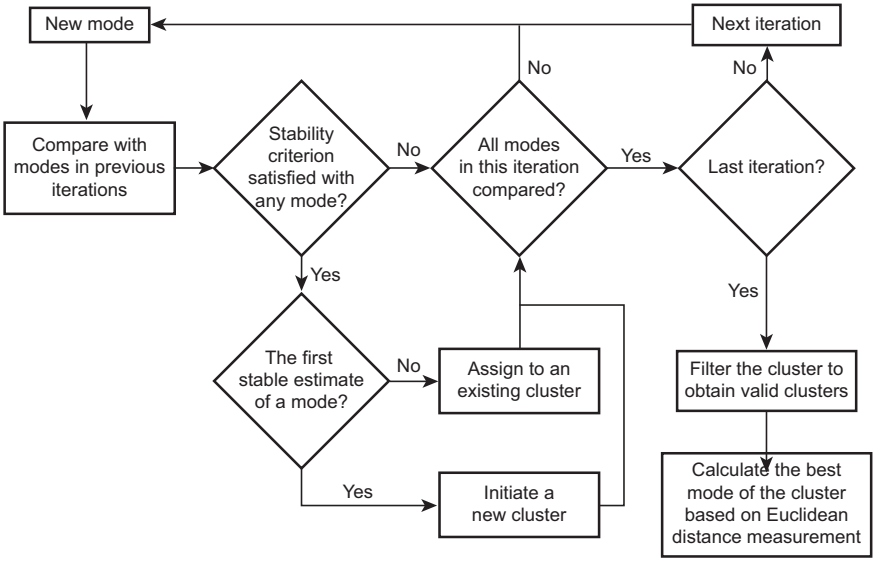

Second Approach (Best Mode Based)

It is worth noting that in the first approach the stability diagram is still being developed in the classical manner of comparing modes from an iteration to those obtained in the previous iteration. In this sense, one ignores the information provided in earlier iterations, using only information provided in the current and the iteration previous to the current one.

In the proposed second approach, each mode, whether computational or physical, is assigned to a cluster. For each cluster a best mode is selected amongst all the estimates that form the cluster. Unlike the first approach, every new mode is now compared to these best modes representing various clusters. Depending on whether the comparison criterion is satisfied, a mode is assigned to an existing cluster or assigned to an entirely new cluster. Further, every time a mode is assigned to a cluster, the best mode of that cluster is recalculated. When modes from all the iterations have been considered, cluster filtering is done to separate computational and physical modes.

The flowchart for this approach is shown in Fig. 3.

Fig. 3. Flowchart for Best Mode based approach

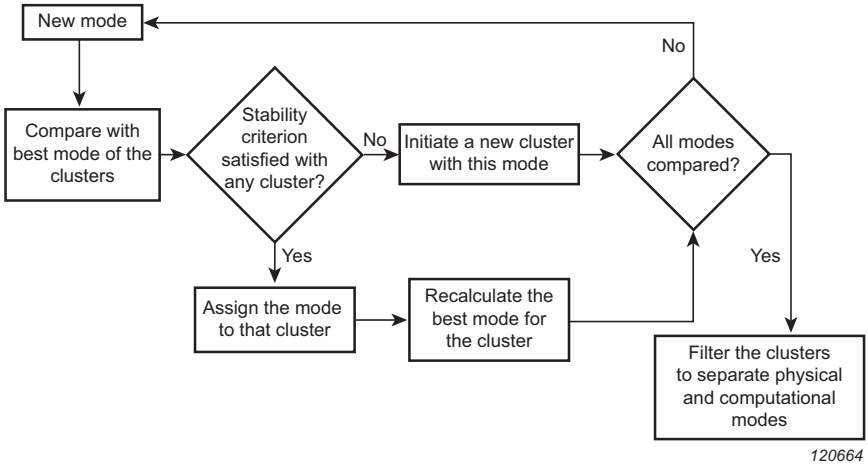

The best modes representing the valid clusters obtained after the filtering stage are also the automatically selected modes. It should be noted that the process of determining the best modes is based on a Euclidian distance measure, in the same manner as the previously discussed first approach. The advantage of this approach

over the first approach is that it utilizes the complete information obtained from various iterations while calculating the stability of a mode and not just the previous iteration. This results in stability diagrams that are more informative in comparison. This aspect is further illustrated by means of examples in the next section.

Studies on Analytical Dataset

Fig. 4 shows a stability diagram obtained for an analytical rotor dataset. The stability diagram is prepared in the traditional manner. The symbols in the stability diagram represent:

+ New Mode
× Stable Frequency
* Stable Frequency and Damping
∇ Stable Frequency and Vector
◊ Stable Mode with Frequency, Damping and Vector all stable

Fig. 4. Stability diagram (0 – 100 Hz frequency range)

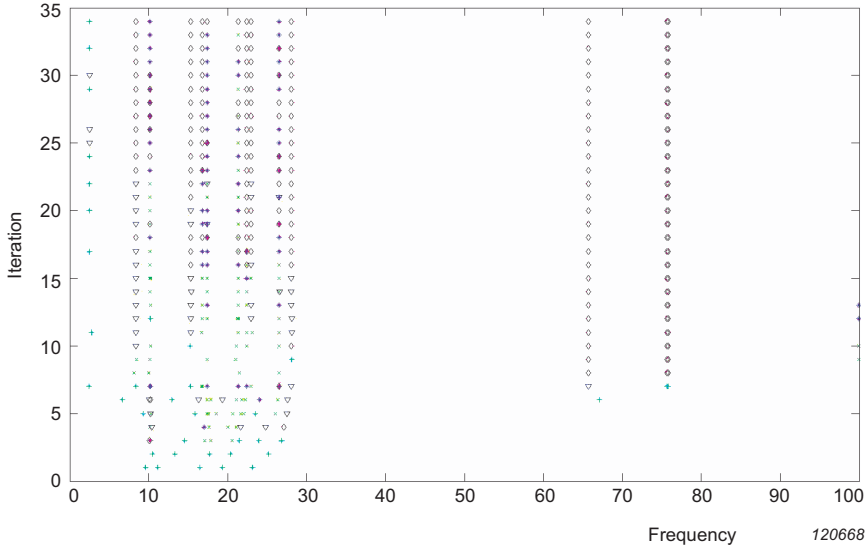

Damping and frequency values for the various modes in the frequency range of interest are shown in Table 1. Modes indicated in gray are repeated or closely spaced modes. It is worth noting that this is a pretty complex system with plenty of modes that are not only repeated modes but also very similar in terms of damping.

Table 1. Modal Parameters of the Analytical System

Analytical		Traditional Stability Diagram based approach		Best Mode based approach	
Freq (Hz)	**Damping (%)**	**Freq (Hz)**	**Damping (%)**	**Freq (Hz)**	**Damping (%)**
2.4780	0.0156				
8.3549	0.0525	8.3549	0.0526	8.3549	0.0521
10.1817	0.0640			10.1816	0.0641
10.1818	0.0640				
15.3281	0.0963	15.3281	0.0965	15.3281	0.0965
16.7506	0.1052	16.7506	0.1052	16.7506	0.1052
16.7554	0.1053	16.7555	0.1054	16.7554	0.1052
17.4015	0.1093			17.4014	0.1100
17.4016	0.1093			17.4015	0.1079
21.3338	0.1340			21.3351	0.1330
21.3338	0.1340				
22.3986	0.1407	22.3986	0.1409	22.3986	0.1409
22.4139	0.1408	22.4140	0.1410	22.4140	0.1410
22.9526	0.1442	22.9526	0.1445	22.9526	0.1445
26.5336	0.1667			26.5326	0.1664
26.5337	0.1667			26.5337	0.1667
28.0756	0.1764	28.0755	0.1765	28.0755	0.1765
65.6950	0.4128	65.6950	0.4128	65.6950	0.4128
75.6227	0.4752	75.6227	0.4752	75.6227	0.4752
75.8303	0.4765	75.8303	0.4765	75.8303	0.4765

Once the stability diagram is prepared, the user has to select various modes based on this stability diagram. This procedure might be easy in case of certain modes (for example modes at 65.6, 75.6 and 75.8 Hz) while extremely difficult in others (repeated roots at 16.75 and 22.39 Hz; see Fig. 5, which shows the zoomed in portion of stability diagram between 16.5 – 23 Hz). The user has to rely significant amount of experience and knowledge in order to recover these modes.

Fig. 5. Stability diagram (16.5 – 23 Hz frequency range)

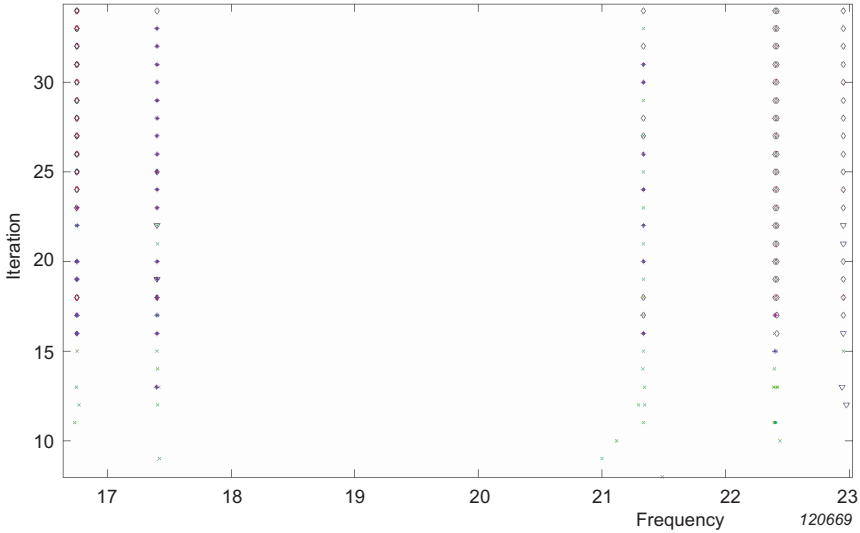

Fig. 6 shows the results of the automatic mode selection done using the traditional stability diagram based approach. Using this approach, a total of 11 modes are obtained which are listed in Table 1 and indicated as solid red diamonds with arrows in Fig. 6. Nine modes are not identified, all of them being repeated modes (except the mode at 2.47 Hz). On observing the stability diagram, particularly for these modes, it is evident that in the case of these modes the stability is not very good. In such a case, the user will not generally pick these modes at all or will try to improve his estimation.

Fig. 7 shows the stability diagram prepared using the Best Mode based approach. A total of 17 modes are identified using this approach, which signifies an improvement over previous approach. It should be noted that similar stability criteria are used for both approaches. The advantage of the second approach of being able to identify more modes than the previous approach comes from the fact that it takes into consideration information available from all previous iterations. Thus, there is less chance of missing a good mode in this approach as stability level is decided with respect to the best mode of the cluster, not with respect to the immediately previous mode (which can be an outlier). This can be illustrated in this case by the fact that stability levels for certain modes (like repeated modes at 10.18, 17.4, 26.53 Hz, etc.) is improved in comparison to when stabilities are

Fig. 6. Traditional stability diagram approach based automatic mode selection

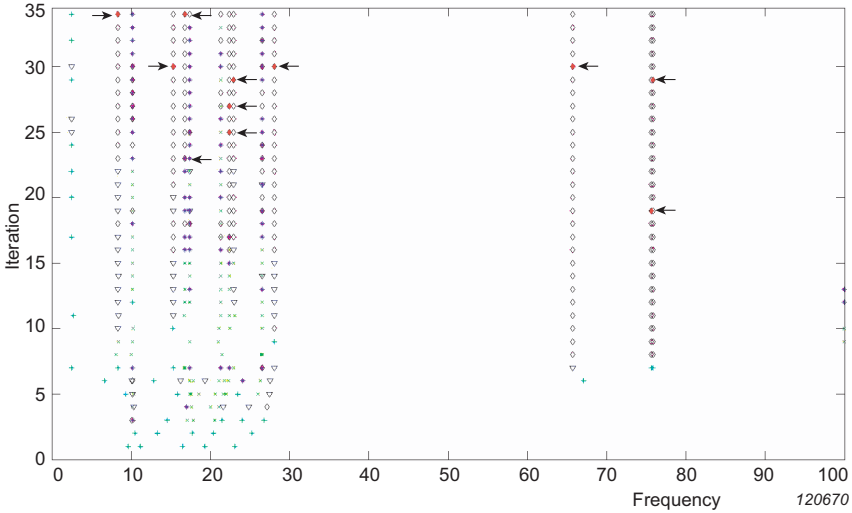

Fig. 7. Best mode based stability diagram and automatic mode selection

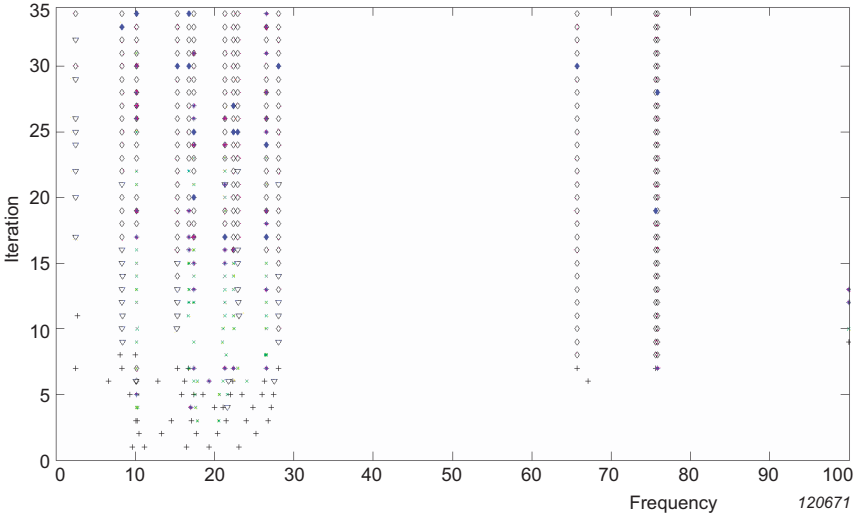

calculated in a traditional manner on an iteration by iteration basis. This results in a better stabilization diagram and ultimately more modes being identified. Yet another aspect of the Best Mode based approach is illustrated by observing stabilization levels around 2.47 Hz using both approaches. Although, this mode is not identified using either approaches, it is clear that the Best Mode based approach is more indicative of the presence of this mode than the previous approach. On the basis of this knowledge the user might carry out modal parameter estimation with different algorithmic parameters in order to obtain this mode.

Cluster based approaches, as suggested in the paper, also provide a way to obtain statistical data about the automatically chosen modal parameter estimates. Since each cluster contain various estimates of the same mode, one can easily obtain statistical measures such as mean and standard deviation. These statistics provide useful additional information about the estimated parameters that can also aid the user in making a better decision regarding parameter estimation. Table 2 and Table 3 list the mean and standard deviation for the various estimates obtained using the two approaches.

Table 2. Cluster Statistics for Traditional Stability Diagram based approach

Traditional Stability Diagram Based Approach					
Frequency (Hz)			**Damping (% Critical)**		
Automatically Selected Mode	**Mean**	**Standard Deviation**	**Automatically Selected Mode**	**Mean**	**Standard Deviation**
8.3549	8.3548	2.0833e-04	0.0526	0.0521	0.0017
15.3281	15.3280	1.8492e-04	0.0965	0.0961	8.1028e-04
16.7506	16.7506	3.6995e-04	0.1052	0.1053	0.0011
16.7555	16.7554	2.3726e-04	0.1054	0.1058	0.0012
22.3986	22.3987	1.8765e-04	0.1409	0.1412	0.0013
22.4140	22.4140	2.0279e-04	0.1410	0.1411	8.9666e-04
22.9526	22.9527	2.2956e-04	0.1445	0.1435	0.0016
28.0755	28.0756	4.3830e-04	0.1765	0.1765	0.0016
65.6950	65.6950	3.6534e-004	0.4128	0.4127	6.5969e-004
75.6227	75.6227	3.3838e-004	0.4752	0.4752	6.8348e-004
75.8303	75.8305	0.0013	0.4765	0.4763	6.6210e-004

Table 3. Cluster Statistics for Best Mode based approach

Best Mode Based Approach					
Frequency (Hz)			Damping (% Critical)		
Automatically Selected Mode	Mean	Standard Deviation	Automatically Selected Mode	Mean	Standard Deviation
8.3549	8.3548	1.9935e-04	0.0521	0.0518	0.0019
10.1818	10.1817	4.3937e-004	0.0654	0.0650	0.0015
15.3281	15.3281	3.8048e-004	0.0965	0.0967	0.0014
16.7506	16.7505	1.9212e-004	0.1052	0.1055	8.6664e-004
16.7554	16.7554	2.2717e-004	0.1052	0.1058	0.0012
17.4014	17.4018	3.9135e-004	0.1100	0.1094	0.0012
17.4015	17.4017	1.4785e-004	0.1079	0.1086	0.0018
21.3351	21.3338	1.7139e-004	0.1330	0.1344	6.6254e-004
22.3986	22.3986	2.1752e-004	0.1409	0.1414	0.0017
22.4140	22.4141	7.2579e-004	0.1410	0.1416	0.0024
22.9526	22.9527	2.3311e-004	0.1445	0.1435	0.0016
26.5336	26.5336	3.6793e-004	0.1664	0.1666	0.0021
26.5337	26.5336	7.0399e-004	0.1667	0.1667	2.4026e-004
28.0755	28.0756	5.5423e-004	0.1765	0.1768	0.0018
65.6950	65.6949	3.9947e-004	0.4128	0.4128	6.9889e-004
75.6227	75.6227	4.6055e-004	0.4752	0.4752	6.7244e-004
75.8303	75.8306	0.0014	0.4765	0.4763	6.5138e-004

Conclusions

The stability diagram is an important tool in the modal parameter estimation phase whose understanding and utilization is highly subjective, depending on expertise and user know-how. In this paper, two methods (Traditional Stability Diagram based and Best Mode based) for automating the modal parameter estimation process are suggested. Both methods involve the formation of clusters on a logical rule based approach. However, these methods differ in the manner of formulating the clusters. The Best Mode based method utilizes complete information available from all previous iterations while preparing the stability diagram, unlike the Traditional Stability Diagram based method which uses information only from the immediately previous iteration. On formation of clusters, a Euclidian distance based automatic mode selection process is carried out to identify the best mode representing the cluster.

It is shown by means of studies performed on an analytical dataset that the Best Mode based method results in a stability diagram which is more informative in comparison to the one obtained with the traditional approach. This is indicative in terms of improved stability of certain modes which do not stabilize sufficiently enough while using the traditional approach and hence the risk of not choosing these modes is lessened. The automatic mode selection procedure also works satisfactorily. It is further observed that even in cases where a mode might not have been automatically selected using either approach the Best Mode method is more indicative of its presence than the Traditional Stability Diagram method.

Automatic mode selection is a desired tool in the modal analysis community as it can not only help in reducing the overall analysis and estimation time but also lends itself very well to online monitoring, which holds the key to many applications including Structural Health Monitoring, Flutter Analysis, etc. The studies conducted in this paper suggest positively that proposed methods are capable of automating the modal parameter estimation process. It does not, however, rule out user know-how completely, because there are still several factors that require user intervention; for example, choice of parameter estimation algorithm, frequency range of interest, choice of input references, etc. Nonetheless, this is a valuable tool as once the initial parameters (like frequency range, number of references, etc.) for the estimation algorithm are chosen, the automatic mode selection procedure makes the rest of the process faster, easier, reliable and independent of user interaction.

Although the two methods gave satisfactory results on a complicated dataset, the need to further test them with real-life data cannot be overlooked. It is important to note that since these methods are based on the implementation of certain logical rules, their success depends on the robustness of these rules under various conditions. Thus, it is important to test these methods more rigorously by means of several real-life datasets so as to make them fulfil the original goals of automatic mode selection, which include being robust, reliable and involving no user interaction.

References

[1] Pappa, R.S., James, G.H., Zimmerman, D.C.; "Autonomous Modal Identification of the Space Shuttle Tail Rudder", *Journal of Spacecrafts and Rockets, Vol. 35(2), 1998*.

[2] Pappa, R.S., Elliot, K.B., Schenk, K.; "Consistent-Mode Indicator for Eigensystem Realization Algorithm", *Journal of Guidance, Control and Dynamics, Vol. 16(5), pp. 852–858, 1993*.

[3] Chhipwadia, K.S., Zimmerman, D.C., James, G.H.; "Evolving Autonomous Modal Parameter Estimation", *Proc. 17th IMAC, Kissimmee, FL, February 1999*.

[4] Scionti, M., Lanslots, J., Goethals, I., Vecchio, A., Van der Auweraer, H., Peeters, B., De Moor, B.; "Tools to Improve Detection of Structural Changes from In-Flight Flutter Data", *Proc. 8th International Conference on Recent Advances in Structural Dynamics, Southampton, UK, 2003.*

[5] Goethals, I., De Moor, B.; "Model reduction and Energy Analysis as a Tool to Detect Spurious Modes", *Proc. ISMA International Conference on Noise and Vibration Engineering, Katholieke Universiteit Leuven, Belgium, 2002.*

[6] Verboven, P., Parloo, E., Guillaume, P., van Overmeire, M.; "Autonomous Modal Parameter Identification based on Statistical Frequency-Domain Maximum Likelihood Approach", *Proc. 19th IMAC, Kissimmee, FL, February 2001.*

[7] Vanlanduit, S., Verboven, P., Guillaume, P., Schoukens, J.; "An Automatic Frequency Domain Modal Parameter Estimation Algorithm", *Journal of Sound and Vibration, Vol. 265, pp. 647–661, 2003.*

[8] Verboven, P., Parloo, E., Guillaume, P., Van Overmeire, M.; "Autonomous Structural Health Monitoring – Part I: Modal Parameter estimation and Tracking", *Mechanical Systems and Signal Processing, Vol. 16(4), pp. 637–657, 2002.*

[9] Scionti, M., Lanslots, J.; "Stabilization Diagrams: Pole Identification Using Fuzzy Clustering Techniques", *Advances in Engineering Software, Vol. 36, pp. 768–779, 2005.*

[10] Carden, E.P., Brownjohn, J.M.W.; “Fuzzy Clustering of Stability Diagrams for Vibration-Based Structural Health Monitoring”, *Computer-Aided Civil and Infrastructure Engineering, Vol. 23, pp. 360–372, 2008.*

[11] Goethals, I., Vanluyten, B., De Moor, B.; “Reliable Spurious Mode Rejection using Self Learning Algorithms”, *Proc. ISMA International Conference on Noise and Vibration Engineering, Katholieke Universiteit Leuven, Belgium, 2006.*

[12] Brown, D.L., Allemang, R.J., Zimmerman, R.D., Mergeay, M.; “Parameter Estimation Techniques for Modal Analysis”, *SAE Paper Number 790221, SAE Transactions, Vol. 88, pp. 828–846, 1979.*

[13] Vold, H., Rocklin, T.; “The numerical implementation of a multi-input modal estimation algorithm for mini-computers”; *Proc. 1st IMAC, Orlando, FL, November 1982.*

[14] Vold, H., Kundrat, J., Rocklin, T., Russell, R.; “A multi-input modal estimation algorithm for mini-computers”, *SAE Transactions, Vol. 91, Number 1, pp. 815–821, January, 1982.*

[15] Richardson, M., Formenti, D.; “Parameter estimation from frequency response measurements using rational fraction polynomials”, *Proc. 1st IMAC, Orlando (FL), USA, 1982.*

[16] Allemang, R.J., Brown, D.L., Fladung, W.A.; “Modal parameter estimation: A Unified Matrix Polynomial Approach”, *Proc. 12th IMAC, Honolulu, Hawaii, January, 1994.*

[17] Allemang, R.J., Brown, D.L.,; “A unified matrix polynomial approach to modal identification”, *Journal of Sound and Vibration, Volume 211, Number 3, pp. 301–322, April 1998.*

[18] Allemang, R.J., Phillips, A.W.; “The unified matrix polynomial approach to understanding modal parameter estimation: an update”, *Proc. ISMA International Conference on Noise and Vibration Engineering, Katholieke Universiteit Leuven, Belgium, 2004.*

[19] Verboven, P., Guillaume, P., Cauberghe, B., Parloo, E., Vanlanduit, S.; “Stabilization Charts and Uncertainty Bounds for Frequency-Domain Linear Least Squares Estimators”, *Proc. 21st IMAC, Kissimmee, FL, 2003.*

[20] Phillips, A.W., Allemang, R.J., Pickrel, C.R.; “Estimating Modal Parameters from Different Solution Sets”, *Proc. 16th IMAC, Santa Barbara, CA, 1998.*

[21] Juang, J.N., Pappa, R.S.; “An Eigensystem Realization Algorithm for modal parameter identification and model reduction”, *AIAA Journal of Guidance, Control and Dynamics 8 (4), pp. 620–627, 1985.*

[22] Longman, R.W., Juang, J.N.; “Recursive form of the eigensystem realization algorithm for system identification”, *AIAA Journal of Guidance, Control and Dynamics 12 (5), pp. 647–652, 1989.*

[23] Ibrahim, S.R., Mikulcik, E.C.; “A method for direct identification of vibration parameters from the free response”, *Shock and Vibration Bulletin, Vol. 47 (4), pp. 183–198, 1977.*

[24] Pappa, R.S.; “Some statistical performance characteristics of the ITD modal identification algorithm”, *AIAA Paper Number 82–0768, p. 19, 1982.*

[25] Zhang, L., Kanda, H., Brown, D.L., Allemang, R.J.; “A polyreference frequency domain method for modal parameter identification”, *American Society of Mechanical Engineers, Paper No. 85-DET-106, 1984.*

[26] Lembregts, F., Leuridan, J.L., Zhang, L., Kanda, H.; “Multiple input modal analysis of frequency response functions based on direct parameter identification”, *Proc. 4th IMAC, Los Angeles, CA, Feb 1986.*

[27] Lembregts, F., Leuridan, J.L., H. Van Brussel; “Frequency domain direct parameter identification for modal analysis: state space formulation”, *Mechanical Systems and Signal Processing, 4 (1) (1989) pp. 65–76.*

[28] Phillips, A.W., Allemang, R.J.; “Additional Mechanisms for Providing Clear Stabilization (Consistency) Diagrams”, *Proc. ISMA International Conference on Noise and Vibration Engineering, Katholieke Universiteit Leuven, Belgium, 2008.*

Previously issued numbers of Brüel & Kjær Technical Review

(Continued from cover page 2)

1 – 2001 The Influence of Environmental Conditions on the Pressure Sensitivity of Measurement Microphones
Reduction of Heat Conduction Error in Microphone Pressure Reciprocity Calibration
Frequency Response for Measurement Microphones – a Question of Confidence
Measurement of Microphone Random-incidence and Pressure-field Responses and Determination of their Uncertainties
1 – 2000 Non-stationary STSF
1 – 1999 Characteristics of the vold-Kalman Order Tracking Filter
1 – 1998 Danish Primary Laboratory of Acoustics (DPLA) as Part of the National Metrology Organisation
Pressure Reciprocity Calibration – Instrumentation, Results and Uncertainty
MP.EXE, a Calculation Program for Pressure Reciprocity Calibration of Microphones
1 – 1997 A New Design Principle for Triaxial Piezoelectric Accelerometers
A Simple QC Test for Knock Sensors
Torsional Operational Deflection Shapes (TODS) Measurements
2 – 1996 Non-stationary Signal Analysis using Wavelet Transform, Short-time Fourier Transform and Wigner-Ville Distribution
1 – 1996 Calibration Uncertainties & Distortion of Microphones.
Wide Band Intensity Probe. Accelerometer Mounted Resonance Test
2 – 1995 Order Tracking Analysis
1 – 1995 Use of Spatial Transformation of Sound Fields (STSF) Techniques in the Automative Industry

Special technical literature

Brüel & Kjær publishes a variety of technical literature that can be obtained from your local Brüel & Kjær representative.

The following literature is presently available:

- Catalogues
- Product Data Sheets

Furthermore, back copies of the Technical Review can be supplied as listed above. Older issues may be obtained provided they are still in stock.

www.bksv.com

BV 0064 – 11 ISSN 0007 – 2621

HEADQUARTERS: Brüel & Kjær Sound & Vibration Measurement A/S
DK-2850 Nærum Denmark · Telephone: +45 7741 2000 · Fax: +45 4580 1405
www.bksv.com · info@bksv.com

Brüel & Kjær

Local representatives and service organisations worldwide